



Comparison between Core-collapse Supernova Nucleosynthesis and Meteoric Stardust Grains: Investigating Magnesium, Aluminium, and Chromium

Jacqueline den Hartogh^{1,9} , Maria K. Petö¹ , Thomas Lawson^{1,2,3,9} , Andre Sieverding^{4,5} , Hannah Brinkman^{1,6} ,
Marco Pignatari^{1,2,3,9} , and Maria Lugaro^{1,7,8}

¹ Konkoly Observatory, Research Centre for Astronomy and Earth Sciences, Eötvös Loránd Research Network (ELKH), Konkoly Thege Miklós út 15-17, H-1121 Budapest, Hungary; maria.lugaro@csfk.org

² E.A. Milne Centre for Astrophysics, Department of Physics and Mathematics, University of Hull, HU6 7RX, UK

³ Joint Institute for Nuclear Astrophysics—Center for the Evolution of the Elements, USA

⁴ School of Physics and Astronomy, University of Minnesota, Minneapolis, MN 55455, USA

⁵ Physics Division, Oak Ridge National Laboratory, P.O. Box 2008, Oak Ridge, TN 37831-6354, USA

⁶ Graduate School of Physics, University of Szeged, Dom tér 9, Szeged, 6720, Hungary

⁷ ELTE Eötvös Loránd University, Institute of Physics, Budapest 1117, Pázmány Péter sétány 1/A, Hungary

⁸ School of Physics and Astronomy, Monash University, VIC 3800, Australia

Received 2021 June 4; revised 2021 December 7; accepted 2021 December 21; published 2022 March 17

Abstract

Isotope variations of nucleosynthetic origin among solar system solid samples are well documented, yet the origin of these variations is still uncertain. The observed variability of ^{54}Cr among materials formed in different regions of the protoplanetary disk has been attributed to variable amounts of presolar, chromium-rich oxide (chromite) grains, which exist within the meteoritic stardust inventory and most likely originated from some type of supernova explosion. To investigate if core-collapse supernovae (CCSNe) could be the site of origin of these grains, we analyze yields of CCSN models of stars with initial masses 15, 20, and 25 M_{\odot} , and solar metallicity. We present an extensive abundance data set of the Cr, Mg, and Al isotopes as a function of enclosed mass. We find cases in which the explosive C ashes produce a composition in good agreement with the observed $^{54}\text{Cr}/^{52}\text{Cr}$ and $^{53}\text{Cr}/^{52}\text{Cr}$ ratios as well as the $^{50}\text{Cr}/^{52}\text{Cr}$ ratios. Taking into account that the signal at atomic mass 50 could also originate from ^{50}Ti , the ashes of explosive He burning also match the observed ratios. Addition of material from the He ashes (enriched in Al and Cr relative to Mg to simulate the make-up of chromite grains) to the solar system's composition may reproduce the observed correlation between Mg and Cr anomalies, while material from the C ashes does not present significant Mg anomalies together with Cr isotopic variations. In all cases, nonradiogenic, stable Mg isotope variations dominate over the variations expected from ^{26}Al .

Unified Astronomy Thesaurus concepts: Core-collapse supernovae (304); Explosive nucleosynthesis (503); Nucleosynthesis (1131); Stellar nucleosynthesis (1616); Interstellar medium (847); Meteorites (1038); Meteors (1041); Stellar astronomy (1583)

1. Introduction

Isotopic differences of nucleosynthetic origin are observed among meteorite groups and primitive meteorite components that formed in the solar system. For example, spinel-hibonite spherules and “normal” calcium- and aluminum-rich inclusions (CAIs) do not show nucleosynthetic variability, while ultra-refractory platy hibonite crystals and CAIs with fractionation and unidentified nuclear effects (also known as FUN CAIs) do. This has been interpreted as a record of progressive homogenisation of dust and gas in the inner regions of the protoplanetary disk via turbulent mixing and thermal heating during the T-Tauri phase of the Sun (Mishra & Chaussidon 2014; Pignatari et al. 2018, 2019; Jacquet et al. 2019). Nucleosynthetic isotope variations are also observed among bulk compositions of meteorites and planetary objects, which implies that large-scale isotopic heterogeneities, inherited from the proto-solar nebula and/or formed during the evolution of the protoplanetary disk, have been preserved.

These variations, however, are hard to connect to nucleosynthetic signatures from specific stellar sources. A number of scenarios have been developed to explain such a connection. These range from isotopic differences inherited from an inhomogeneous molecular cloud (Dauphas et al. 2002; Burkhardt et al. 2019; Nanne et al. 2019), late processes acting on a once-homogenized material in the inner regions of the protoplanetary disk (Dauphas et al. 2008; Regelous et al. 2008; Trinquier et al. 2009; Burkhardt et al. 2012; Poole et al. 2017), and/or new material added to the protoplanetary disk after the formation of the Sun (Van Kooten et al. 2016; Schiller et al. 2018).

Solids from the protoplanetary disk not only display variation in bulk isotopic compositions but often also display a discontinuity (gap). For the isotopes of many elements (e.g., Cr, Ti, Mo, Ru), meteorite types are well separated into two groups. Because of this compositional gap, nucleosynthetic isotope variations are often called the “isotopic dichotomy” of the protoplanetary disk (Warren 2011). Materials assumed to have formed in the outer solar system are associated with enrichment in neutron-rich isotopes of intermediate-mass and iron-group elements, such as ^{48}Ca , ^{50}Ti , and ^{54}Cr (see, e.g., Trinquier et al. 2007, 2009; Schiller et al. 2018), neutron-capture-affected isotopes such as those of Mo and Ru (see, e.g., Budde et al. 2016; Kruijjer et al. 2017; Nanne et al. 2019), and

⁹ NuGrid Collaboration, <http://nugridstars.org>.

other isotopes of explosive nucleosynthetic origin such as ^{58}Ni (Nanne et al. 2019) and ^{92}Nb (Hibiya et al. 2019), as compared to materials assumed to have formed in the inner solar system;¹⁰ see, e.g., Budde et al. (2016), Kruijer et al. (2017), Nanne et al. (2019), Hibiya et al. (2019), and the review by Kleine et al. (2020).

The nucleosynthetic source of these enrichments has been attributed to supernovae (SNe) but the exact origin is still unclear (e.g., Hartmann et al. 1985; Dauphas et al. 2010). The formation of Jupiter’s core (Helled et al. 2014; Kruijer et al. 2017) or a pressure maximum in the disk leading to such formation (Brasser & Mojzsis 2020) have been invoked as the barrier that kept these two reservoirs well separated in the early solar system.

The chromium isotopes are exceptionally useful to deconvolve the origin of planetary-scale nucleosynthetic isotope variation in iron-group elements because Cr has four stable isotopes (at atomic masses 50, 52, 53, and 54), which allows us to obtain two ratios after mass-fractionation effects are removed with internal normalization. Furthermore, it appears that the main feature of the Cr anomaly, i.e., enrichment and depletion of the most neutron-rich isotope (^{54}Cr), is driven by a single, well-identified mineral carrier. Dauphas et al. (2010) and Qin et al. (2010) identified this carrier phase as Cr oxide (with variable structure, but mostly chromium-rich Mg spinel, here referred to as chromite) and found that variable abundance of such presolar grains can explain all the variations observed among bulk meteorites. Nittler et al. (2018) provided high-precision Cr data on these presolar chromite, confirming the previously assumed high $^{54}\text{Cr}/^{52}\text{Cr}$ ratios (up to 80 times the solar ratio). Nittler et al. (2018) compared their data to a limited number of SN models and concluded that the observations are better explained by models of electron-capture SNe (Wanajo et al. 2013) and rare, high-density type Ia SNe (Woosley 1997) than by models of core-collapse supernovae (CCSNe) by Woosley & Heger (2007).¹¹

Interestingly, ^{54}Cr variations among bulk meteorites and planetary objects may also correlate with mass-independent ^{26}Mg isotope variations (Larsen et al. 2011; Van Kooten et al. 2016). The observed variation in the $^{26}\text{Mg}/^{24}\text{Mg}$ stable isotope ratio can be due to a heterogeneous distribution of the short-lived radionuclide, ^{26}Al (which decays to ^{26}Mg with a half-life of 0.717 Myr) along the protoplanetary disk, or to variations in stable ^{26}Mg and/or ^{24}Mg abundances, or both. Jacobsen et al. (2008) and Kita et al. (2013) argue for a homogeneous Mg isotope distribution in the solar system. Larsen et al. (2011) proposed that the apparent positive correlation between ^{54}Cr and ^{26}Mg anomalies among planetary objects is the result of progressive thermal processing of in-falling ^{26}Al -rich molecular cloud material toward the inner regions of the disk. This in return results in preferential loss of thermally unstable and isotopically anomalous dust. Alternatively, Van Kooten et al. (2016) suggested that the apparent positive correlation between

^{54}Cr and ^{26}Mg may represent “unmixing” of distinct dust populations with different thermal properties. Old, thermally processed, presolar, homogeneous dust could mix with fresh, thermally unprocessed, SN-derived dust, which formed shortly before the solar system. This newly condensed dust is then preferentially lost from the inner regions of the protoplanetary disk. Because of the high significance of this apparent correlation and its possible interpretations, we also make a first attempt to address it here from the point of view of stellar modeling by exploring the Al and Mg isotopic composition of the specific CCSN regions that match the nucleosynthesis anomalies in presolar chromite grains. With simple mixing relations, we investigate if these CCSN abundances can generate any significant variation in ^{26}Al or stable Mg isotopes among planetary objects. This is a simplified first attempt to linking stardust data to meteorites and planetary objects because it assumes that such Al and Mg abundances are carried in the chromite grains and/or similar carriers enriched in Al. While this is a possible scenario, there is no evidence for it yet as there have been no Mg or O isotope studies on chromite presolar grains.

Here, we compare the predictions from three sets of CCSN models, from stars of initial masses 15, 20, and 25 M_{\odot} and solar metallicity, to the chromite data to evaluate the role of CCSNe as potential sources of chromite grains in the large-scale heterogeneity of the protoplanetary disk. We will also compare the abundances of the stable isotopes of Cr, Al, and Mg and ^{26}Al in three sets of CCSN models and evaluate the isotopic abundances and ratios as a function of the enclosed stellar mass. Our aims are as follows: first, to identify ^{54}Cr production sites within CCSNe that may match the chromite grains; second, to evaluate the ^{26}Al production and Mg isotope compositions associated with such ^{54}Cr production sites; and, third, to investigate if the Al and Mg abundances of the CCSN region of potential origin of the chromite grains could produce variation in ^{26}Al or ^{26}Mg isotopes among planetary objects (under the simple assumption described above). Furthermore, we compare the ^{26}Al production in the CCSN models to the ^{26}Al signatures in the presolar grains from CCSN that we found in the literature, in order to put our analysis of potential Al and Mg abundances in chromite grains into the wider context of CCSN stardust grains in general.

The structure of the paper is as follows. In Section 2 we briefly describe the specifics of the CCSN data sets and outline their differences. A comparison of the total yields for the nine Al, Mg, and Cr isotopes is presented in Section 3, and in Section 4 we present a comparison between the CCSN models and the observed Cr isotopic compositions of stardust grains, as well as the comparison of the CCSN models to $^{26}\text{Al}/^{27}\text{Al}$ in other presolar CCSN grains. In our discussion, in Section 5, we present the effects of uncertainties associated with neutron-capture reaction rates, an analysis on the Al and Mg isotopic composition of the ^{54}Cr production sites, and a comparison between modeled ejecta compositions and the meteoritic data. Our conclusions are presented in Section 6.

2. Methods

CCSNe are explosions associated with the death of massive stars that process their initial composition through a sequence of hydrostatic nuclear burning stages until an Fe core is formed (see Langer 2012, for an extensive review). The self-consistent modeling of the explosion mechanism is still challenging and

¹⁰ Material from the outer and inner solar system are represented, respectively, by (i) carbonaceous chondrites and “carbonaceous-type” iron meteorites, collectively referred to as CC; and (ii) ordinary chondrites, lunar and Martian samples, “noncarbonaceous-type” iron meteorites, and various achondrites, collectively referred to as NC.

¹¹ Also, in asymptotic giant branch (AGB) stars neutron-capture processes can enrich the ^{54}Cr relative to the other Cr isotopes. However, the largest anomaly predicted in models of O-rich massive AGB stars does not exceed values in the order of 40%, based on a 6 M_{\odot} model of solar metallicity from (Karakas & Lugaro 2016). Therefore, we can exclude that neutron captures in AGB stars are sources of presolar chromite with these anomalies.

Table 1
Overview of the Details of the Different Yield Sets Included in this Paper

Set	Code for Progenitors	Code for Explosions	Initial Abundances	Solar Metallicity
Lawson et al. (LAW; 2022)	Kepler	Convective engine	GN93	$Z = 0.02$
Sieverding et al. (SIE; 2018)	Kepler	Kepler	L03	$Z = 0.013$
Ritter et al. (RIT; 2018)	MESA	Semianalytical	GN93	$Z = 0.02$
Limongi & Chieffi (LIM; 2018) ^a	FRANEC	FRANEC	AG89 ^b	$Z = 0.02$
Rauscher et al. (RAU; 2002)	Kepler ^c	Kepler	AG89 ^b	$Z = 0.02$
Curtis et al. (CUR; 2019)	Kepler	PUSH	L03	$Z = 0.013$
Sukhbold et al. (SUK; 2016) ^d	Kepler	Kepler (W18 engine)	L03	$Z = 0.013$

Notes. The first three studies are discussed in detail in this work, the last four are only included here and in Section 3.2.

^a This study also investigates the effects of rotation, but we exclude those models in our comparison due to the large uncertainties present in the theory of rotation in stellar evolution (see, e.g., Aerts et al. 2019; den Hartogh et al. 2019; Belczynski et al. 2020).

^b Anders & Grevesse (1989).

^c Progenitor models from Woosley & Weaver (1995) (all other Kepler progenitor models are more recent)

^d We include two models (14.9 and 25.2 M_{\odot}) as shown in the paper; other yields can be found in their online data.

requires three-dimensional (3D), high-resolution simulations, which are currently too expensive to allow us to perform large-scale surveys for nucleosynthesis studies (for recent reviews, see Burrows 2013, Janka et al. 2016, and Müller 2016). Instead, parameterized, spherically symmetric simulations have been employed widely to estimate CCSN nucleosynthesis yields. In such models, the innermost part of the CCSN progenitor is usually not simulated in detail but replaced with an engine that artificially drives the explosion, such as a piston (Woosley & Weaver 1995) or the injection of thermal energy (Limongi & Chieffi 2003), which can be tuned with a few model-specific parameters to yield a desired explosion energy, measured as the kinetic energy at infinity, and remnant mass, which is referred to as the mass cut. In addition to the neutron star that is left behind by the explosion, the mass cut also includes the possibility of fallback, i.e., material that is initially ejected but remains gravitationally bound to the remnant and thus eventually falls back onto it, possibly leading to the formation of a black hole even after a successful explosion (Zhang et al. 2008; Fryer 2009). Recently, models have been developed that treat the evolution of the stellar core in more detail, instead of with an engine, and still achieve explosions in spherically symmetric simulations by different parameterizations (Perego et al. 2015; Sukhbold et al. 2016; Couch et al. 2020). Such models are promising to improve on the simple models mentioned above, but remain to be validated by comparison to multidimensional simulations and observations.

We collected three CCSN yield sets for $^{24,25,26}\text{Mg}$, $^{26,27}\text{Al}$, and $^{50,52,53,54}\text{Cr}$ (Lawson et al., 2022; Ritter et al. 2018; Sieverding et al. 2018), for which we have access to abundance profiles as a function of the stellar mass coordinate. These yield sets are based on one-dimensional (1D) calculations using different stellar-evolution, explosion, and postprocessing codes. We include only models with an initial mass of 15, 20, and 25 M_{\odot} at solar metallicity, since higher mass stars are expected to result in the formation of a black hole without any significant ejection of material processed by explosive nuclear burning (Heger et al. 2003). We exclude the effects on yields by rotation, magnetic fields, and binary evolution as these are not known or too uncertain (Aerts et al. 2019; den Hartogh et al. 2019; Belczynski et al. 2020). The yield sets are listed in Table 1, together with details on codes used for the calculations. For each data set we list in the following

subsections the codes used for the calculations and the details of the initial setups that are important for our comparison.

2.1. Data Set of Lawson et al. (LAW; 2022)

The LAW models are a part of the large data set presented in Fryer et al. (2018), who performed a parameter study over a broad range for SN explosions. Andrews et al. (2020) used these models to study the production of radioactive isotopes relevant for the next generation of facilities for γ -ray astronomy, and provided the complete yields for the full stellar set. Jones et al. (2019b) used the same set to study the production of ^{60}Fe . Here we use the updated yield set based on the same models, but updated by including a recent bug fix (Lawson et al., 2022).

The progenitor stellar-evolution models were calculated with a recent version of the Kepler hydrodynamic code (Weaver et al. 1978; Heger & Woosley 2010), using initial abundances based on Grevesse & Noels (1993, hereafter GN93). The progenitors were postprocessed to obtain the detailed nucleosynthetic results using the Multi-zone Post-Processing Network—Parallel (MPPNP; see Pignatari et al. 2016; Ritter et al. 2018). The explosions of the progenitors are calculated using a 1D code mimicking a 3D convective engine, as described in Herant et al. (1994) and Fryer et al. (1999). The explosion nucleosynthesis is calculated using the Tracer particle Post-Processing Network—Parallel (TPPNP; see Jones et al. 2019b). The difference between MPPNP and TPPNP is that the first also performs mixing of mass shells following the mixing as calculated in the progenitor or explosion model, while the latter does not apply any mixing and may efficiently streamline the postprocessing of trajectories. The same nuclear-reaction package is used from the two postprocessing frameworks.

2.2. Data Set of Sieverding et al. (SIE; 2018)

The progenitor models of SIE were calculated with a slightly older version of the Kepler code than the LAW models. Differences include the neutrino loss rates, as discussed by Sukhbold et al. (2018), and updated photon opacities. Due to these differences, the SIE models show a less massive C/O core and more compact structure than the LAW models. The initial abundances for the progenitors of SIE are based on Lodders (2003, hereafter L03). The explosion was simulated with a piston, as described in Woosley & Weaver (1995). The

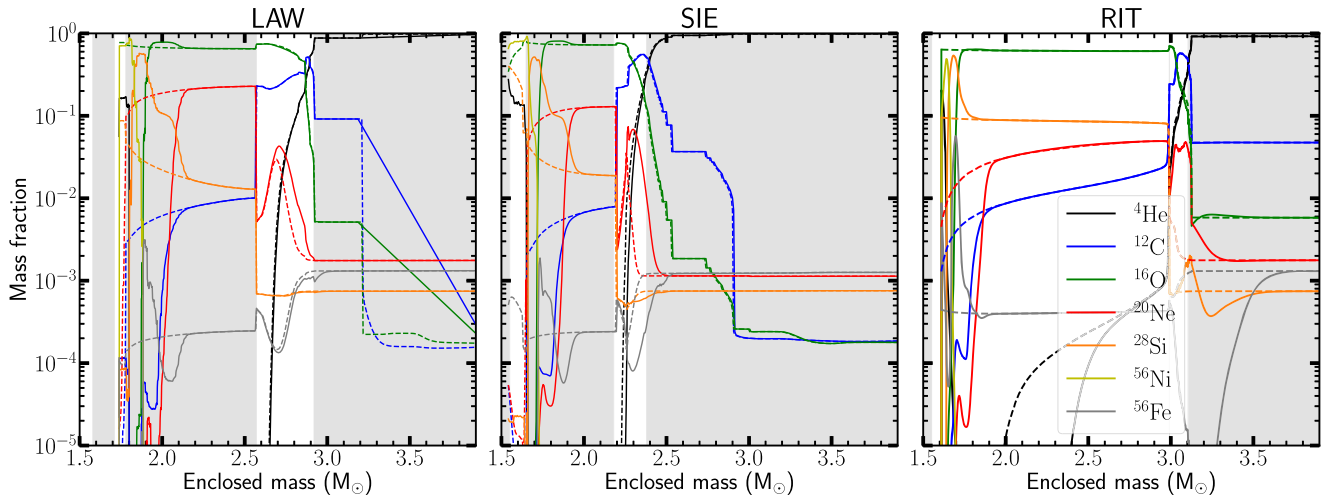


Figure 1. Structure plots showing the three (nondecayed) $15 M_{\odot}$ models with gray and white bands to indicate the different regions (labeled as “ashes” in the text). The more compact structure of SIE compared to LAW is visible when comparing the mass coordinates of the bands. Furthermore, the RIT model shows a different internal structure due to the shell merger. See the [Appendix](#) for the Al, Mg, and Cr isotope plots.

piston is put at the mass cut determined by the position where the entropy per baryon drops below $4 k_B$. The parameters of the piston were adjusted to produce an explosion energy of 1.2×10^{51} erg. All matter outside the mass cut is assumed to be ejected, i.e., no additional fallback is considered.

The explosive nucleosynthesis was postprocessed by Sieverding et al. (2018), who performed a parameter study around the effects of neutrino energies. We include here the models with the highest neutrino energy.

2.3. Data Set of Ritter et al. (RIT; 2018)

The progenitor models of Ritter et al. (2018) were calculated with the MESA stellar-evolution code (Paxton et al. 2011) with initial abundances based on GN93. The explosion models were calculated via a semianalytical approach using the delayed formalism as described in Pignatari et al. (2016), and using the mass cuts from Fryer et al. (2012). The detailed nucleosynthesis was calculated for the progenitor and the explosion with the MPPNP postprocessing code. In the evolution of the $15 M_{\odot}$ star the convective O and C shells merge. This feature can occur during the later phases of stellar evolution, when the different burning shells form close enough to each other to possibly merge. The shell merger in the $15 M_{\odot}$ progenitor model takes place at the end of the core Si-burning phase; see the [Appendix](#) for more details. Shell mergers are often found in 1D and 3D stellar-evolution models (see Müller 2020, for a recent review), and shell-merger events are often initiated shortly before the collapse. Collins et al. (2018) found that 40% of their stellar-evolution models with an initial mass between 16 and $26 M_{\odot}$ start core collapse during an ongoing shell merger.

2.4. Decayed Abundances

We present the isotope abundances and isotopic ratios as a function of stellar mass coordinates for both the progenitor and explosion models. Unless indicated otherwise, in the following figures we show the abundances obtained after decaying all the radioactive isotopes created during the explosion into their respective stable isotope, except for the case of ^{26}Al , as we want to study its production. For the isotopes of interest here, the most relevant decay chain is $^{53}\text{Mn}(\beta^+)^{53}\text{Cr}$ with a half-life

of 3.74 Myr. Its effect on the comparison to the stardust grains will be considered in Section 4.1.

2.5. Nomenclature

In the following sections we define the regions within the stellar model from the envelope toward the core in the following way:

1. If ^4He is the most abundant isotope, the region is called *H ashes* (the gray band located at the highest mass coordinate in the three panels of Figure 1).
2. If ^{12}C and ^{16}O are the most abundant isotopes, the region is called *He ashes* (the white band located at the highest mass coordinate in the three panels of Figure 1).
3. If ^{16}O and ^{20}Ne are the most abundant isotopes, the region is called *C ashes* (the gray band located to the left of the He ashes in the three panels of Figure 1).
4. If ^{16}O and ^{28}Si are the most abundant isotopes, the region is called *Ne ashes* (the white band located to the left of the C ashes in the three panels of Figure 1). The shell-merger region in the $15 M_{\odot}$ RIT model is also labeled as Ne ashes.
5. If ^{28}Si is the most abundant isotope, the region is called *O ashes* (the gray band located to the left of the Ne ashes in the three panels of Figure 1).
6. If ^{56}Ni and ^{56}Fe are the most abundant isotopes, the region is called *Si ashes* (the white band located to the left of the O ashes in the three panels of Figure 1).

This nomenclature represents a simplified structure of the regions within massive stars before explosion, and is often used within the massive-star community. The nomenclature of Meyer et al. (1995) is commonly used in the presolar grain community and, when we compare our version to theirs, identifies mostly the same zones. The main difference is that they name the zone based on the most abundant isotopes, while our names refer back to the main fuel within the region. When putting the two schemes next to each other we get the following: our H ashes are their He/N and He/C zones; our He ashes are their O/C zone; our C ashes are their O/Ne zone; our Ne ashes are their O/Si zone; our O ashes are their Si/S zone; and our Si ashes are their Ni zone.

Table 2
The Burning Phases in the Progenitor and Explosion where the Isotopes of Interest are Created and Destroyed for the 15 M_{\odot} LAW Model

	Progenitor				Explosion			
	Produced in	Via	Destroyed in	Via	Produced in	Via	Destroyed in	Via
^{24}Mg	C, Ne, He	α -cap	He	α -cap	O, Si	Photodis
^{25}Mg	C, Ne, He	N-cap	Ne	Photodis	He	N, α -cap	C	α -cap
^{26}Mg	C, Ne, He	N-cap	Ne	Photodis	He	N-cap	C	α -cap
^{26}Al	C	P-cap	Ne, He	Several	C	P-cap	O	Photodis
^{27}Al	C, Ne	P-cap	O	Photodis	O	Photodis
^{50}Cr	C	P-cap	He	N-cap	O, Si	P-cap	Si	Equi
^{52}Cr	He, C	N-cap	O	Equi	Si	Equi
^{53}Cr	C	N-cap	He	N-cap	He	N-cap	C	N-cap
^{54}Cr	He	N-cap	He	N-cap	C	N-cap

Note. The burning phases are labeled using the definitions which were set in Section 2.5 (the word “ashes” is not repeated). The dominant nucleosynthesis process responsible for the production or destruction of each isotope are also indicated and explained in more detail in the text (“cap” is short for “capture”). This table is specifically for 15 M_{\odot} , which might be where the differences with Table 3 of Woosley et al. (2002) arise. When comparing our table to Curtis et al. (2019), the differences are due to our table excluding radiogenic contributions and including outer layers, which are the exact opposites of the features in the table of Curtis et al. (2019).

3. Yields

We discuss in the first subsection the creation of $^{24,25,26}\text{Mg}$, $^{26,27}\text{Al}$, and $^{50,52,53,54}\text{Cr}$ in massive stars. Our analysis is focused on these nine isotopes and their distribution in CCSN ejecta. The total isotopic yields of the data sets are compared in the second subsection.

3.1. Creation of the Al, Mg, and Cr Isotopes in Massive Stars and Core-collapse Supernovae

We trace the internal structure of the models by plotting the abundance profiles of the mass fractions of ^4He , ^{12}C , ^{16}O , ^{20}Ne , ^{28}Si , ^{56}Ni , and ^{56}Fe as a function of mass coordinate. In Figure 1 we show the structure plots of the 15 M_{\odot} models of LAW, SIE, and RIT. In the Appendix we provide figures of all three initial masses and the three data sets, showing the internal structures and also the final mass fractions of the Mg, Al, and Cr isotopes of the progenitor and explosion models.¹²

Table 2 shows the production and destruction sites of the nine isotopes of interest, plus their dominant reaction paths for the 15 M_{\odot} LAW model. Two reaction paths require explanation: “Photodis” stands for photodisintegration, the process where an incoming photon removes a neutron, proton, or an α particle from the nucleus. “Equi” denotes the production in high-temperature equilibrium conditions when most forward and backward reaction rates are closely matched (Woosley et al. 1973; Chieffi et al. 1998). This usually applies to explosive Si and O burning.

In the following we highlight the most important differences between the models with respect to the production and destruction of the isotopes we are interested in. The 15 M_{\odot} SIE progenitor model shows production and destruction sites (Figure A1) that are comparable to the 15 M_{\odot} LAW model. The 15 M_{\odot} RIT progenitor model, however, experiences a shell merger, which allows for C burning while He burning is still ongoing. Furthermore, the shell merger allows for mixing of Cr isotopes from the deeper layers outwards. In this shell-merger region, the 15 M_{\odot} RIT model shows a higher abundance for ^{20}Mg than ^{25}Mg (the opposite is visible in the LAW and SIE 15

M_{\odot} models), and the presence of $^{50,52}\text{Cr}$ mixed up from deeper layers, which is not taking place in the LAW and SIE 15 M_{\odot} models. The 15 M_{\odot} explosive models of SIE and RIT show more explosive He burning than the 15 M_{\odot} LAW model. This allows for the production of the Mg isotopes and extra destruction of $^{50,52}\text{Cr}$ in the SIE and RIT 15 M_{\odot} models.

The main difference between the 15 and 20 M_{\odot} LAW progenitor models is that the mass cut is higher in the 20 M_{\odot} model (Figure A2), which leads to the exclusion of the Ne ashes from the ejecta. The 20 M_{\odot} SIE model is the only 20 M_{\odot} model including the Ne ashes where ^{26}Al is produced. The 20 M_{\odot} RIT model shows a mass cut similar to the 20 LAW model and a production of ^{26}Al in the C ashes, like the 15 M_{\odot} RIT model. The main difference between the three 20 M_{\odot} models is that they show different amounts of explosive nucleosynthesis. The 20 M_{\odot} LAW explosive model shows no explosive nucleosynthesis involving the nine isotopes in Table 2. The 20 M_{\odot} SIE model, however, shows explosive nucleosynthesis in the inner regions, producing ^{26}Al and $^{50,52}\text{Cr}$. The 20 M_{\odot} RIT model shows explosive nucleosynthesis in the whole star, due to its high temperature compared to the other 20 M_{\odot} models (Figure A4). The explosive He burning in this model is similar to the 15 M_{\odot} RIT model, while the explosive C burning leads to the creation of ^{26}Al and $^{50,52}\text{Cr}$ and the destruction of ^{27}Al and $^{53,54}\text{Cr}$.

The 25 M_{\odot} progenitor models (Figure A3) are similar to the 15 M_{\odot} progenitor models, except for the high mass cut in the upper C ashes in the 25 M_{\odot} RIT model. The other two models show mass cuts below the Ne ashes. In the 25 M_{\odot} explosive models we see explosion nucleosynthesis only in the inner regions of the LAW and SIE 25 M_{\odot} models, and not from explosive He burning. This means most explosive contributions to the nine isotopes of interest are still present. In contrast, the 25 M_{\odot} RIT model only experiences explosive He burning as its mass cut is too high to include the other regions.

3.2. Comparison of the Total Yields

Here we present a comparison of the total yields of seven CCSN data sets (not the net yields, which are calculated as the total yield minus the initial abundance). An overview of the main characteristics of the models by LAW, SIE, and RIT is

¹² All the data used to produce the figures in this paper can be found on Zenodo: [doi:10.5281/zenodo.5822654](https://doi.org/10.5281/zenodo.5822654).

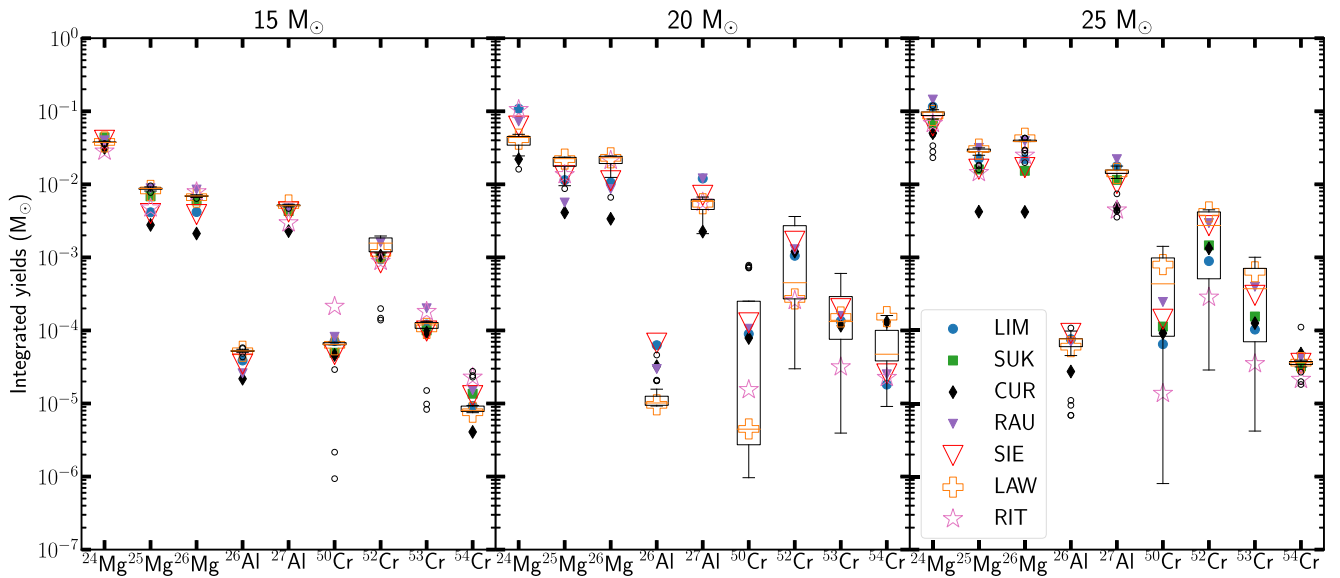


Figure 2. Comparison of the isotope yields of the three CCSN data sets considered in this paper, plus four others found in the literature. The three models of LAW that are considered in this paper and shown in the [Appendix](#) are plotted as orange open crosses. The yields of all the models of LAW are included in the rectangle boxes, where the median values of the models are shown as orange lines. The box plots cover the values between 25% and 75% of all the data points, while the error bars cover 1.5 times the range of the box plot. Any points outside the error bars are shown as open circles. The yield sets are labeled as indicated in [Table 1](#).

given in [Table 1](#), together with other four sets of CCSN models that are available in the literature ([Rauscher et al. 2002](#); [Sukhbold et al. 2016](#); [Curtis et al. 2018](#); [Limongi & Chieffi 2018](#)). The seven sets have been calculated with different 1D stellar-evolution and explosion codes. While this is not meant to be a comprehensive collection of CCSN yields available, it may be considered as indicative of the existing abundance variations obtained from different CCSN models. A comparison of the seven yield sets is presented in [Figure 2](#). We plot the explosive yields of the nine isotopes $^{24,25,26}\text{Mg}$, $^{26,27}\text{Al}$, and $^{50,52,53,54}\text{Cr}$ for all models grouped together according to their stellar masses.

We note that the CUR yields are often the lowest yield for the Mg and Al isotopes. The reason for this is that this study only includes the inner stellar regions in their nucleosynthesis calculations. Parts of the C-ashes region are cut off where the Mg and Al isotopes are abundant (see [Table 2](#)), resulting in an apparent reduction of the total yield of the Mg and Al isotopes compared to other yields. Overall, we find that variations in the production of the nine isotopes in the seven yield sets are roughly one order of magnitude at most. The range of yields in the LAW models appears to cover most other yield sets, thus confirming that the parameter study of [Fryer et al. \(2018\)](#) well represents the uncertainties within 1D CCSN explosions. We discuss in the remaining of this section the isotopes that show variations larger than one order of magnitude in the LAW, SIE, and RIT yields.

The $^{25,26}\text{Mg}$ and $^{26,27}\text{Al}$ yields of LAW are higher than those of SIE in all panels of [Figure 2](#). This is because, according to the LAW models, the central stellar structures are less compact compared to the SIE models (as mentioned in [Section 2.2](#)). Thus the Mg- and Al-rich C ashes of LAW are located at higher mass coordinates than those of SIE.

Among the $15 M_{\odot}$ models (left panel), only the $^{50, 54}\text{Cr}$ yields show a spread of about one order of magnitude (excluding the few outliers of the LAW data set, shown as small circles). The main reason for this is that the RIT model undergoes a shell merger. In this region the $15 M_{\odot}$ RIT model

creates more Cr than the other two $15 M_{\odot}$ models, as the shell merger transfers iron-group elements from the deeper layers into the merged region (see [Figure A1](#) and [Côté et al. 2020](#)).

Among the $20 M_{\odot}$ models (middle panel) again the Cr isotope yields show the largest spread. The lower values of RIT are due to the higher mass cut values compared to the models of LAW and SIE ([Figure A2](#)). This effect is not present in the Mg and Al isotopes, because these isotopes are produced in regions that are not affected by the mass cut. The large spreads in the models by LAW are caused by its large range of values for the mass cuts; see [Fryer et al. \(2018\)](#).

Also among the yields of the $25 M_{\odot}$ models (right panel) the Cr isotopes show the largest range of variations. The spread in the LAW data set is due to differences in the explosion energies. The Cr yields of RIT are again lower, due to its mass cut being higher than in models by LAW and SIE.

In summary, the main differences between the three data sets of LAW, SIE, and RIT are the structural differences between the progenitors of the LAW and SIE data sets, the C–O shell merger in the $15 M_{\odot}$ RIT model, and the higher mass cuts in the 20 and $25 M_{\odot}$ RIT models.

4. Results and Comparison with Presolar Stardust Grains

Grains are formed locally within the CCSN ejecta, and thus we cannot use the total yields as presented in [Section 3.2](#) for the comparison of CCSN yields to presolar chromite grains. Instead, we compare the high-precision grain data of [Nittler et al. \(2018\)](#) to the Cr isotopic ratios versus mass coordinate of the CCSN data sets of LAW, SIE, and RIT ([Figures 3 and 4](#)). The ratios are plotted against the mass coordinates in [Figure 5](#). [Nittler et al. \(2018\)](#) also considered the possibility that the signal at atomic mass 50 represents ^{50}Ti instead of ^{50}Cr and report the $^{50}\text{Ti}/^{48}\text{Ti}$ ratios inferred for five out of the 19 ^{54}Cr -rich grains. Therefore, we also present and discuss here this possibility, while leaving the extended description of the production of the Ti isotopes in CCSNe to future work.

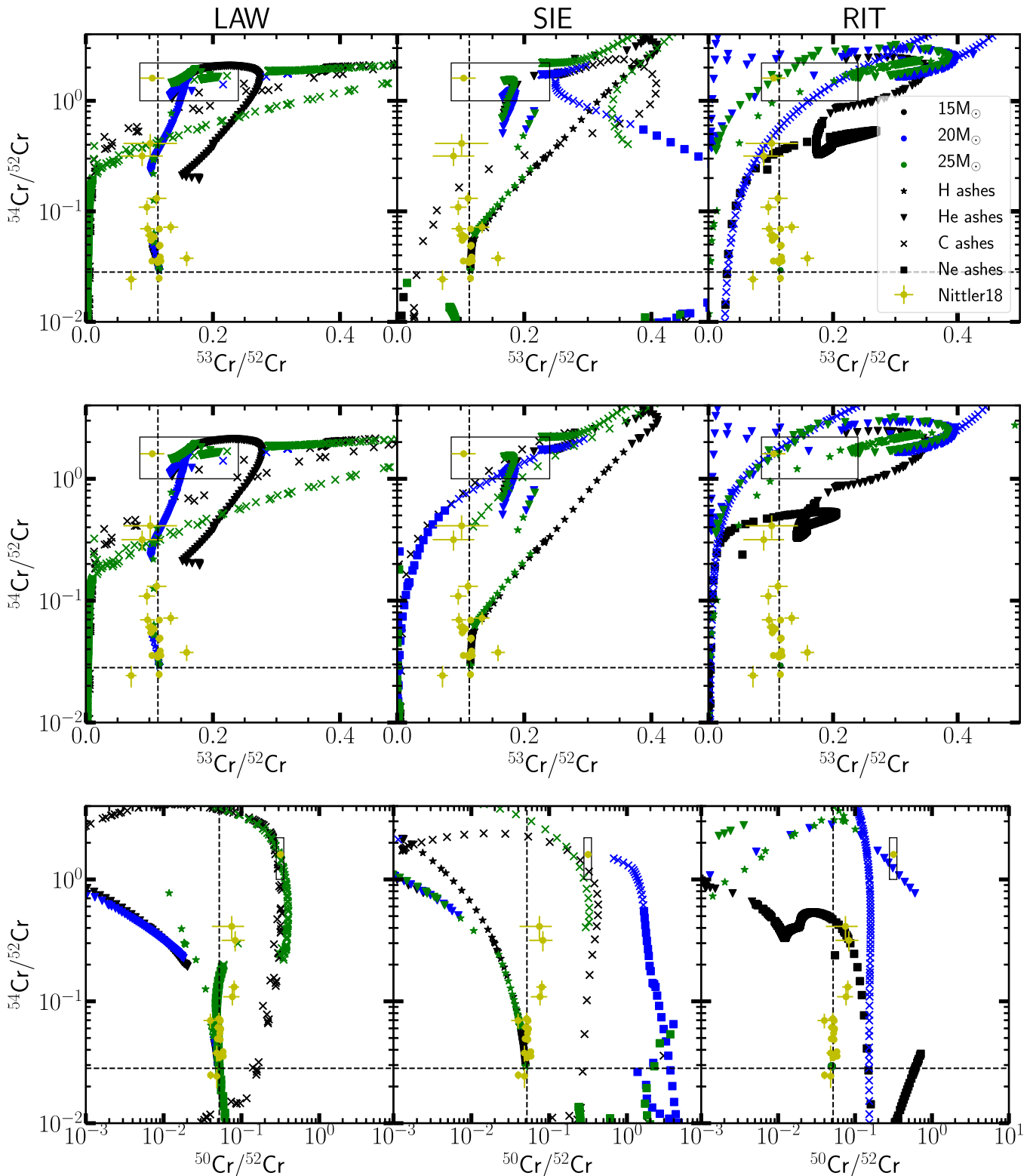


Figure 3. Comparison between the Cr isotopic ratios as measured by Nittler et al. (2018; yellow data points with error bars), and those predicted by LAW, SIE, and RIT (left, middle, and right panels, respectively). Each point of the predictions corresponds to the composition of a mass shell, and different colors and symbols represent different initial masses and ashes, respectively (as indicated in the legend). Note that the symbols for the models are only plotted when the mass regions is O-rich, the relevant condition for the formation of chromite grains. The solar values are shown as black dashed lines. The black boxes around the most anomalous grain 2_37 represent a qualitative estimate of nuclear physics uncertainties as described in the text. The middle row is the same as the top row, except that the abundance of the radioactive ^{53}Mn is not decayed into ^{53}Cr .

Among the models of the LAW data set with different explosion energies, we use one for each initial mass in this section, which has an explosion energy closest to the value of

1.2×10^{51} erg used by Sieverding et al. (2018). The predicted isotopic ratios are calculated using decayed stellar abundances to consider the radiogenic contribution to the final abundances

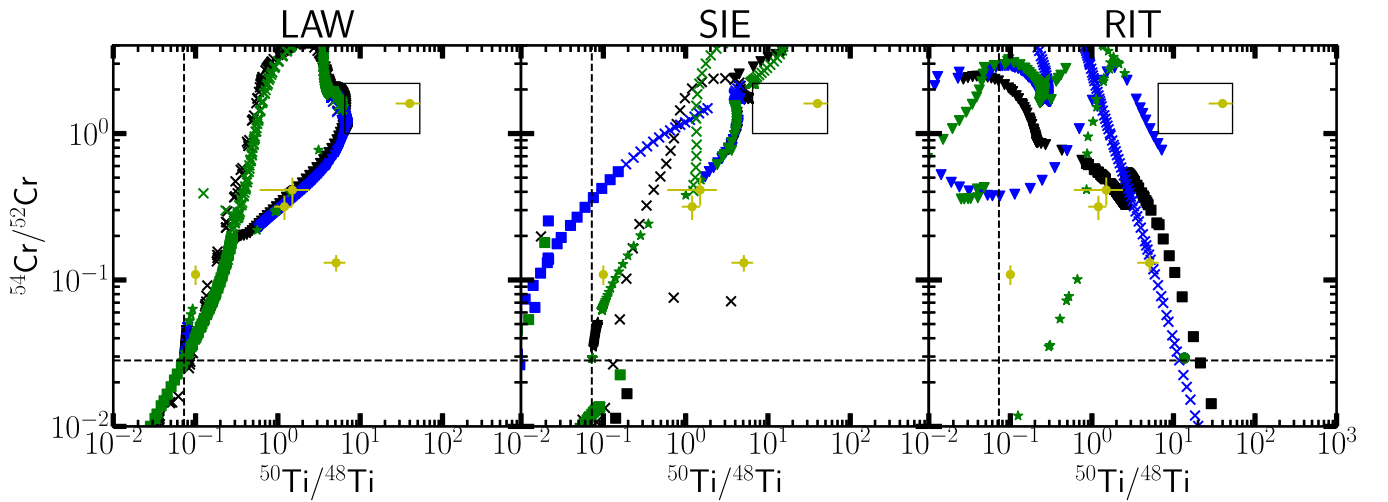


Figure 4. Comparison of the Cr isotopic ratio and Ti isotopic ratio as measured by Nittler et al. (2018) and as predicted isotopic ratios by the three CCSN data sets. The $^{50}\text{Ti}/^{48}\text{Ti}$ ratio is shown instead of $^{50}\text{Cr}/^{52}\text{Cr}$, to investigate whether the mass 50 measurements are due to ^{50}Ti or ^{50}Cr . Colors and symbols are as in Figure 3. The yellow $^{50}\text{Ti}/^{48}\text{Ti}$ data points of Nittler et al. (2018) are calculated using the solar value for $^{50}\text{Cr}/^{52}\text{Cr}$.

of stable isotopes (as explained in Section 2.4), unless indicated otherwise. The boxes in Figures 3 and 4 are explained later in this section, when we precisely locate candidate regions that match the composition of the chromite grains.

We also explore the predicted Al and Mg isotope profiles of the CCSN models as a function of mass coordinate. In Figure 6 we show the $^{26}\text{Al}/^{27}\text{Al}$ ratio profiles of the CCSN models in comparison to the highest values determined for presolar grains of likely CCSN origin, such as SiC type-X grains (e.g., Gropman et al. 2015) and Group 4 presolar oxides (e.g., Nittler et al. 2008).

4.1. Chromite Grains

In Figures 3 and 4 we compare the presolar chromite data of Nittler et al. (2018) to the three data sets of the CCSN model predictions. The predicted Cr ratios as shown in Figures 3 and 4 vary over orders of magnitude, as the different Cr isotopes are created and destroyed in different regions of the progenitor and its explosion (see figures in the Appendix and Table 2). Each data point of the CCSN data sets in Figures 3 and 4 corresponds to one numerical zone in a model, and we do not allow for mixing between zones. Only a few mass shells within each model can reach the stardust data points and are also O-rich (symbols in the figures), the condition necessary to form the chromite grains, as opposed to C-rich (not shown in the figures). We focus our discussion on finding a possible region that has a composition that matches the grain 2_37 (Nittler et al. 2018), which has the most anomalous $^{54}\text{Cr}/^{52}\text{Cr}$ and $^{50}\text{Cr}/^{52}\text{Cr}$ ratios of the grains in this data set. Less extreme values may be explained by dilution effects due to mixing with less processed material in the outer layers of the star, or with material in the interstellar matter (ISM; see e.g., Zinner 2014). First, we consider if a possible exact match of the models to the composition of 2_37 exists, and, second, we take into consideration in the discussion some of the uncertainties due to nuclear physics. These uncertainties are represented in Figures 3 and 4 by the boxes around grain 2_37 and are described in detail below.

We start by considering the top and bottom panels of Figure 3. For the three LAW models, the O-rich regions that can match the $^{54}\text{Cr}/^{52}\text{Cr}$ ratio of 2_37 are the He ashes and C

ashes (triangles and crosses in the top-left panel of Figure 3). Between these two compositions, the He ashes are located close to the required solar value of the $^{53}\text{Cr}/^{52}\text{Cr}$ ratio, while the C ashes provide a wide range of values for $^{53}\text{Cr}/^{52}\text{Cr}$. The C ashes, however, match the $^{50}\text{Cr}/^{52}\text{Cr}$ ratio of 2_37, while the $^{50}\text{Cr}/^{52}\text{Cr}$ ratio of the He ashes are at least one order of magnitude lower than in 2_37 (bottom-left panel of Figure 3). Note, that while the He ashes of the $20 M_{\odot}$ match both the $^{54}\text{Cr}/^{52}\text{Cr}$ and $^{53}\text{Cr}/^{52}\text{Cr}$ ratio of the grains, the $^{50}\text{Cr}/^{52}\text{Cr}$ is almost three orders of magnitude too low.

We reach the same conclusions when considering the three SIE models (middle panels of Figure 3), although the match is slightly worse than for the LAW models. When the $^{54}\text{Cr}/^{52}\text{Cr}$ ratio is matched in the He and C ashes, the $^{53}\text{Cr}/^{52}\text{Cr}$ ratio is at least 50% higher than the solar ratio. When the $^{53}\text{Cr}/^{52}\text{Cr}$ ratio in the C ashes is equal to the solar ratio, the $^{54}\text{Cr}/^{52}\text{Cr}$ ratio is lower than observed in 2_37. For the $^{50}\text{Cr}/^{52}\text{Cr}$ ratio, as in the case of LAW, the 2_37 data point can only be reached in the C ashes. The Ne ashes of the $20 M_{\odot}$ model reach values larger than in 2_37 in the $^{50}\text{Cr}/^{52}\text{Cr}$ (three times larger than in 2_37) and $^{53}\text{Cr}/^{52}\text{Cr}$ ratio (four times larger than in 2_37). $^{54}\text{Cr}/^{52}\text{Cr}$, on the other hand, is at least two times lower than in 2_37.

The Cr yields of the RIT models differ significantly from LAW and SIE (see Section 3). The C, He and H ashes of the RIT $25 M_{\odot}$ model reach the 2_37 $^{54}\text{Cr}/^{52}\text{Cr}$ ratio, but only for the He and H ashes is the $^{53}\text{Cr}/^{52}\text{Cr}$ ratio also matched. None of the mass shells in this model reach the $^{50}\text{Cr}/^{52}\text{Cr}$ ratio of 2_37. The C ashes of the $20 M_{\odot}$ model reach the 2_37 $^{54}\text{Cr}/^{52}\text{Cr}$ ratio, while the $^{53}\text{Cr}/^{52}\text{Cr}$ ratio is two times higher than the solar value observed in the grain. As for the $^{50}\text{Cr}/^{52}\text{Cr}$ ratio, the He ashes within the $20 M_{\odot}$ model have a composition very close to the grains, while the other parts of the ejecta do not. In the case of the $15 M_{\odot}$ model we do not find any region that matches the grain Cr composition.

As mentioned in Section 2.4, in the figures so far we have always presented results for abundances after radioactive decay. However, excluding the radiogenic contributions can make a difference in the case of ^{53}Cr because of the decay of ^{53}Mn . The time between the CCSN and the formation of grains is currently unknown (see, e.g., Sarangi & Cherchneff 2015). If the grains are created long enough after the explosion for all

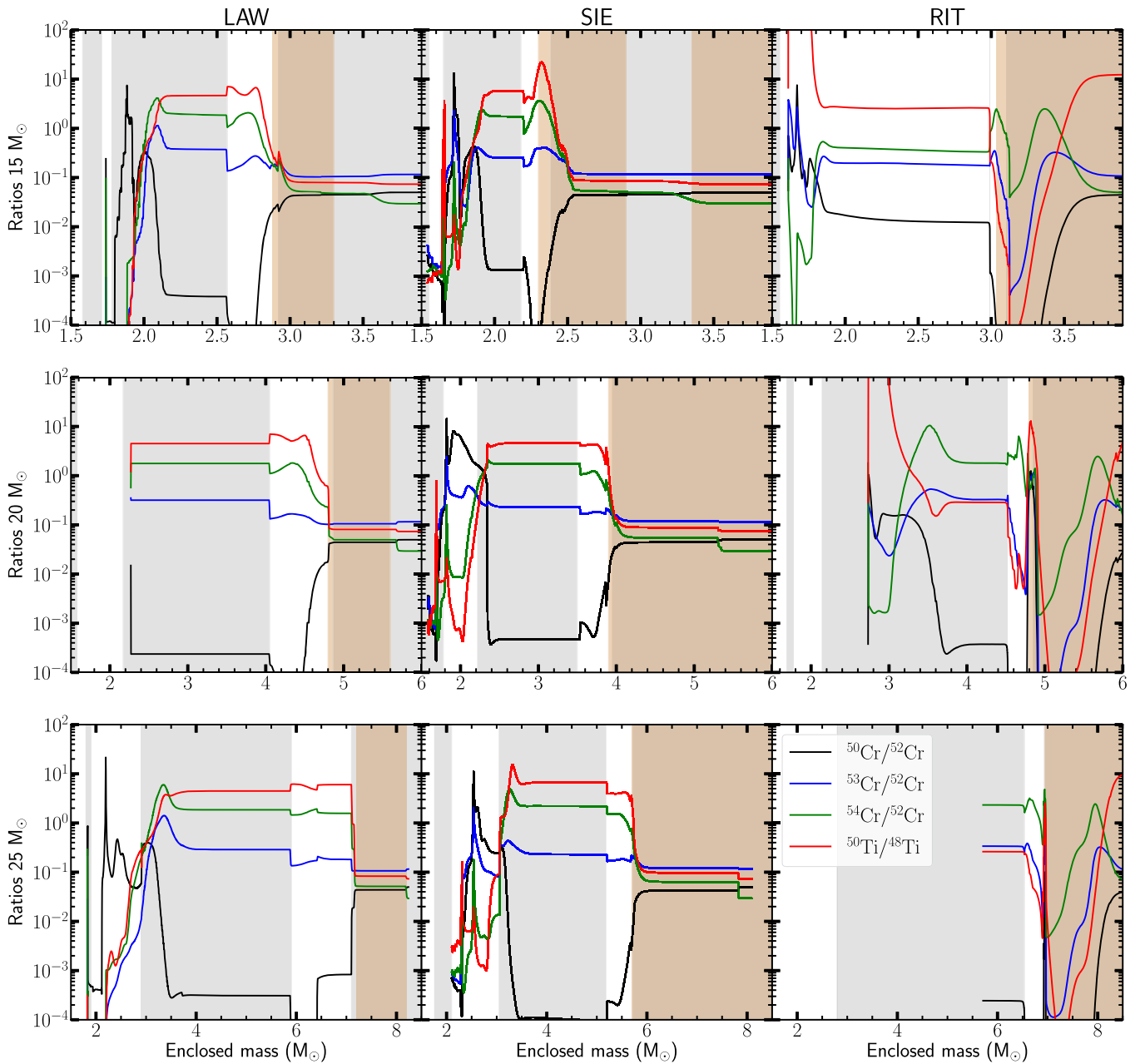


Figure 5. Cr and Ti isotopic ratios of all CCSN prediction (from top to bottom: $15 M_{\odot}$, $20 M_{\odot}$, and $25 M_{\odot}$) after the explosion. The red regions are C-rich, and the gray and white bands indicate the different burning phases, following the nomenclature of Section 2.5.

radioactive isotopes to decay and/or if the radioactive isotopes behave chemically in the same way as their daughter, then they are incorporated into the grains and contribute therein to the abundance of the stable isotopes and the decayed results apply. However, ^{53}Mn has a relatively long half-life of 3.74 Myr so it might be present in the grains; Mn is more volatile than Cr (Lodders 2003); and Mn does not constitute a major element in the spinel structure of the refractory Cr-oxide grains (Dauphas et al. 2010). Therefore, we also show in the middle row of Figure 3 the predicted isotopic ratios for the case that the dust grains have formed before ^{53}Mn has decayed.¹³ When comparing the top and middle panels of Figure 3 we see that

the radiogenic contribution from ^{53}Mn generally does not affect the ratios in regions that are relevant for the comparison to the grains, except for the Ne and C ashes in all the SIE models and the $20 M_{\odot}$ RIT model. In some of the mass shells within these regions, the nondecayed $^{53}\text{Cr}/^{52}\text{Cr}$ ratios are smaller by factors of a few relative to the decayed values, and closer to 2–37.

An ambiguity in the data of Nittler et al. (2018) is that these authors were unable to distinguish between ^{50}Cr and ^{50}Ti at atomic mass $A = 50$.¹⁴ Therefore, it is unclear whether the excess (above the solar ratio) of $^{50}\text{Cr}/^{52}\text{Cr}$ ratio in the five grains is due to ^{50}Cr or ^{50}Ti . For this reason, we also compare our models in relation to the $^{50}\text{Ti}/^{48}\text{Ti}$ ratio; see Figure 4.

¹³ None of the other isotopic ratios discussed here present an effect due to radiogenic decay, except for the $^{57}\text{Fe}/^{56}\text{Fe}$ ratio, which only shows minor differences in the most central O-rich regions.

¹⁴ The authors also checked for ^{50}V and found that there is no V present in the grains.

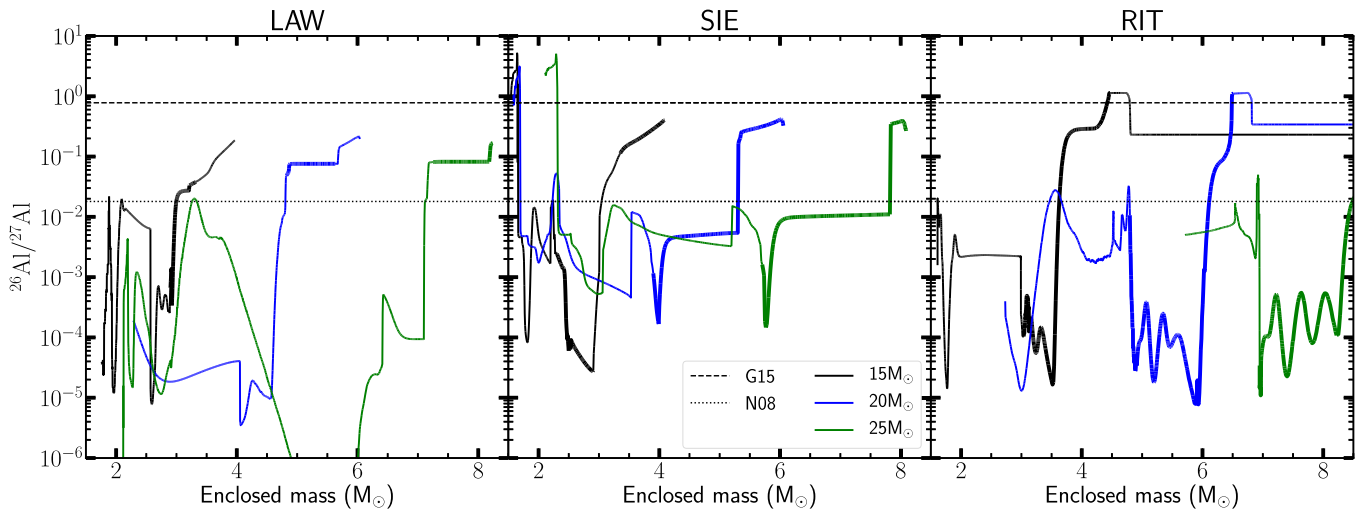


Figure 6. The $^{26}\text{Al}/^{27}\text{Al}$ ratio is shown for the sets of stellar models, while the dashed line is the upper limit of SiC type-X (SiC-X) and graphite data by Groomman et al. (2015) and the dotted line the maximum limit of the four Group 4 grains of Nittler et al. (2008). The thick line segments indicate the C-rich regions and the thin line segments the O-rich regions.

None of the three LAW models is able to reach the $^{50}\text{Ti}/^{48}\text{Ti}$ ratio as found in 2_37. However, the C ashes of the $15 M_{\odot}$ model and the He ashes of the $20 M_{\odot}$ model are only about a factor of three too low. The $15 M_{\odot}$ SIE model reaches the 2_37 value in its C-rich He ashes. The other SIE models only approach the $^{50}\text{Ti}/^{48}\text{Ti}$ of 2_37, with either their He or C ashes. The shell-merger region of the $15 M_{\odot}$ RIT model is able to reach the $^{50}\text{Ti}/^{48}\text{Ti}$ value of 2_37; however, the $^{54}\text{Cr}/^{52}\text{Cr}$ ratio in that region is at least two orders of magnitude lower than in 2_37. The $20 M_{\odot}$ RIT model also approaches the $^{50}\text{Ti}/^{48}\text{Ti}$ value of 2_37, but again the $^{54}\text{Cr}/^{52}\text{Cr}$ ratio is too low.

It is clear from the above analysis that it is impossible to identify large regions within the CCSN models that match three of the four isotopic ratios of the 2_37 grain shown in Figures 3 and 4. Therefore, we now try to identify regions that match the grain when taking into consideration uncertainties due to nuclear physics. In Figures 3 and 4, the grain 2_37 abundances are plotted within boxes. We defined these boxes as a reasoned qualitative estimate of the total uncertainty combining both the grain measurement error and the nuclear physics uncertainties affecting stellar model predictions, as discussed in more detail in Section 5.1.

Specifically, the different axes of the boxes are set as follows:

1. $^{50}\text{Cr}/^{52}\text{Cr}$: ^{50}Cr is mainly created in explosive O and Si burning (see Table 2), and these burning phases are typically not affected by nuclear physics uncertainties.¹⁵ For the $^{50}\text{Cr}/^{52}\text{Cr}$ box we therefore use the measurement of 2_37 and its error bar: 0.317 ± 0.033 .
2. $^{50}\text{Ti}/^{48}\text{Ti}$: the reaction-rate tests in Section 5.1 show that this ratio can change from ~ 4 to ~ 15 when considering neutron-capture rate uncertainties (i.e., a factor ~ 3.7) in the region close to the 2_37 value (Figure 8). Therefore, we use this factor to extend the lower error bar of the lowest value of $^{50}\text{Ti}/^{48}\text{Ti}$ in 2_37, which is 27. The lower limit of the box is thus 7.2. For the upper limit of the box we use the upper error bar of the value of 2_37.

¹⁵ See, e.g., the sensitivity study by Parikh et al. (2013) for Type Ia SNe, where these processes are active, which shows that ^{50}Cr is not affected by reaction-rate variations.

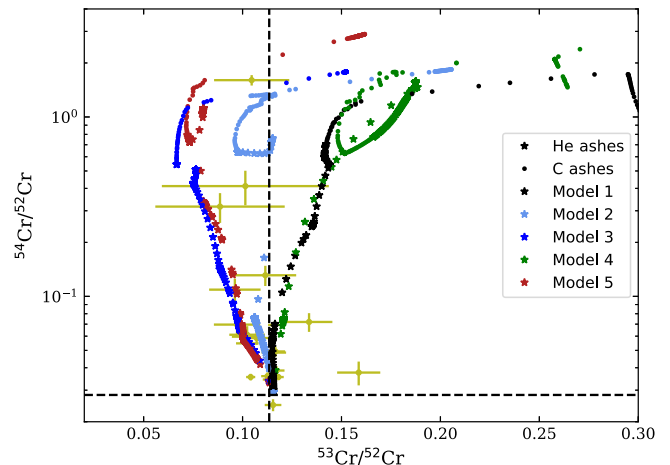


Figure 7. Cr isotopic compositions resulting from the five $20 M_{\odot}$ models calculated using different Cr neutron-capture rates, as listed in the top half of Table 4. The reference model is Model 1. As in Figure 3 the yellow points are the grains from Nittler et al. (2018).

3. $^{53}\text{Cr}/^{52}\text{Cr}$: we used the same reasoning as for $^{50}\text{Ti}/^{48}\text{Ti}$. The uncertainty factor resulting from the reaction-rate tests in Section 5.1 is ~ 2 (Figure 7). We use this factor to extend the upper error bar of 2_37, as the model data is located at higher values.
4. $^{54}\text{Cr}/^{52}\text{Cr}$: for this ratio we extended both the upper and lower error bars of 2_37, as the model data is located at both at higher and lower values than the value of 2_37. The total variation is of a factor of ~ 2 (Figure 7).

Note that for sake of simplicity we did not consider possible effects on ^{52}Cr . This isotope is at the denominator of all the isotopic ratios, therefore changing its abundance would shift all the ratios by the same factor, resulting in a straight line passing through 2_37 rather than a box.

In Table 3, we report the mass coordinates of the predicted model ratios, which are located within the boxes as shown in Figures 3 and 4, and using Figure 5 to identify the mass coordinates. We also list the ashes in which these mass coordinates are located for both the decayed or nondecayed cases. Finally, we list the overlap regions considering mass 50

Table 3
Mass Coordinates (in M_{\odot}) at which the Predicted Ratio is within the Boxes in Figures 3 and 4

	$^{54}\text{Cr}/^{52}\text{Cr}$ vs. $^{50}\text{Cr}/^{52}\text{Cr}$	$^{54}\text{Cr}/^{52}\text{Cr}$ vs. $^{53}\text{Cr}/^{52}\text{Cr}$	$^{54}\text{Cr}/^{52}\text{Cr}$ vs. $^{50}\text{Ti}/^{48}\text{Ti}$	Overlap	Ashes
LAW					
15 M_{\odot}	2.02	2.02, 2.57–2.61, 2.74–2.78	2.58–2.61, 2.77–2.78	^{50}Cr : 2.02	C
15 M_{\odot}				^{50}Ti : 2.58–2.61, 2.77–2.78	He
20 M_{\odot}	...	4.05–4.50	4.05–4.19, 4.47–4.50	^{50}Ti : 4.05–4.19, 4.47–4.50	He
25 M_{\odot}	3.12–3.15	5.88–7.10	6.43–6.44	^{50}Ti : 6.43–6.44	He
SIE					
15 M_{\odot}	1.87–1.88	1.87–1.89, 2.23–2.26	2.36–2.38	^{50}Cr : 1.87–1.88	C
20 M_{\odot}	...	2.28–2.34, 2.44–3.75
25 M_{\odot}	...	3.13, 4.80–5.57	4.80–5.20	^{50}Ti : 4.80–5.20	C (, He)
RIT					
15 M_{\odot}	...	3.04–3.06, 3.32–3.34
20 M_{\odot}	4.86	3.24–3.29, 5.61–5.64
25 M_{\odot}	...	6.54, 6.76–7.00

Note. The reported ranges cover solutions derived both for the decayed and nondecayed abundances. The overlap is defined as the overlap between $^{54}\text{Cr}/^{52}\text{Cr}$ vs. $^{53}\text{Cr}/^{52}\text{Cr}$ and either $^{50}\text{Cr}/^{52}\text{Cr}$ or $^{50}\text{Ti}/^{48}\text{Ti}$ vs. $^{53}\text{Cr}/^{52}\text{Cr}$. The location of the overlap is labeled by the ashes it is located in, and all overlap regions are indicated in Figure 9.

as either Cr or Ti, and these regions are indicated in Figure 9 with red dots.

Table 3 shows that for all models we are able to identify a region in which the predicted ratio can be found within the box of $^{54}\text{Cr}/^{52}\text{Cr}$ versus $^{53}\text{Cr}/^{52}\text{Cr}$. However, not all the models reach one of the other two boxes which include an atomic mass 50 isotope. For five models an overlap between the $^{54}\text{Cr}/^{52}\text{Cr}$ versus $^{53}\text{Cr}/^{52}\text{Cr}$ mass range and at least one of the atomic mass 50 boxes can be found. The box around ^{50}Ti is larger than the box around ^{50}Cr due to the stronger sensitivity to reaction-rate uncertainties. We find a higher number of overlap regions for the box around ^{50}Ti (four) than for the box around ^{50}Cr (two). We note that while an update of the reaction rates that affect the $^{50}\text{Ti}/^{48}\text{Ti}$ ratio could lead to smaller boxes and thus a lower number of overlap regions, the location of these regions would not change. Specifically, the overlap regions that involve $^{50}\text{Cr}/^{52}\text{Cr}$ are always located within the C ashes, while for $^{50}\text{Ti}/^{48}\text{Ti}$ they are located in the He ashes and one in the C ashes. Based on this analysis, the CCSN He ashes and the C ashes are both possible sites of origin for the Cr-rich grains. In the case of the C ashes, it would most likely represent ^{50}Cr . In the case of the He ashes, the signal at atomic mass 50 would most likely represent ^{50}Ti . This is in agreement with Table 2, in which we show that ^{50}Cr is produced in the C ashes, while it is destroyed in the He ashes.

In all three LAW models we have identified overlap regions, as well as in the 15 and 25 M_{\odot} SIE models. We were unable to do so for the 20 M_{\odot} SIE model, likely because the temperature is higher in the region in the 20 M_{\odot} SIE model, where the $^{54}\text{Cr}/^{52}\text{Cr}$ ratio falls within the box around 2_37, than in the same region in the 20 M_{\odot} LAW model. In none of the RIT models were we able to identify overlap regions. In the 15 M_{\odot} model the reason for this is that the shell merger and the explosive He burning due to the temperature peak produce the Cr isotopes in different ratios than in the other models. These two processes take place in the regions where the overlap is found in the LAW and SIE 15 M_{\odot} models. The 20 M_{\odot} RIT model experiences higher temperatures in the C and He ashes

during the explosion (see Figure A4) also leading to different Cr isotopic ratios. For the 25 M_{\odot} RIT model the main issue is the high mass cut, which excludes those regions in the ejecta where we find the overlap regions in the LAW and SIE models.

We also looked at the other models in the data set of Lawson et al. (2022), shown as box plots in Figure 2, which include a variety of values for the explosion energy and the mass cut. The 15 M_{\odot} models show little variability of the relevant isotopic ratios, while the 20 M_{\odot} models show differences in all isotopic ratios close to the mass cut. However, this region does not match the Cr isotopic composition of 2_37. The variations in the 25 M_{\odot} models are larger and present at more regions than in the 15 and 20 M_{\odot} models. Most differences between the models, however, are small and fall within the uncertainty boxes in Figures 3 and 4, and therefore would not lead to more overlap regions than the ones already listed in Table 3. The exception is that several 25 M_{\odot} models with high explosive energies provide a new overlap region, as their $^{50}\text{Ti}/^{48}\text{Ti}$ ratio reaches into the 2_37 box within the He ashes. This overlap region does not alter our findings that the isotope at atomic mass 50 is likely ^{50}Ti in the He ashes and ^{50}Cr in the C ashes.

The analysis above is based on comparison to the most anomalous grain 2_37, and we justified this choice above by considering that less extreme values may be explained by invoking some dilution effect due to mixing with less processed material. However, it is interesting to check if the overall picture above would significantly change if we aimed at matching the two grains that are the second and third most anomalous in the $^{54}\text{Cr}/^{52}\text{Cr}$ ratios.

In the case of the LAW and SIE models, these grains could be matched by considering the C ashes of the 15 and 25 M_{\odot} models or the He ashes of the 20 M_{\odot} models, and the He ashes of the 15 M_{\odot} for the LAW model. In this case the atomic mass 50 is always only matched as ^{50}Ti . The only difference between these two sets of solutions is that in the case of SIE, only the nondecayed abundances can match the two grains (as otherwise the addition of ^{53}Mn produces too high abundance at atomic mass 53), while in the case of LAW both the decayed and the

nondecayed predictions match the grains. Finally, these two grains can also be matched by the composition of the Ne ashes (shell merger) of the RIT 15 M_{\odot} model, in which case the isotope at atomic mass 50 could be either ^{50}Cr or ^{50}Ti . We note that all the solutions for all the three most anomalous grains reported in this section require relatively narrow CCSN mass regions. Other SN studies that have attempted to explain the presolar Cr-oxide data share the same problem of localised grain condensation (see, e.g., Nittler et al. 2018; Jones et al. 2019a).

Furthermore, we note that, as reported by Nittler et al. (2018), the $^{57}\text{Fe}/^{56}\text{Fe}$ ratio of the grains is compatible within the error bar to the solar value except for one grain, called 2_81. The models can reproduce solar $^{57}\text{Fe}/^{56}\text{Fe}$ ratios but only for very small specific ranges of mass coordinates, for example in the O and C ashes at mass coordinates 2.2 and 2.9 M_{\odot} for the LAW 25 M_{\odot} model. This would make it very difficult for such a signature to be predominant in the grains. However, the error bars on the $^{57}\text{Fe}/^{56}\text{Fe}$ ratios are very large, of the order of the measured anomaly itself, because the overall abundance of Fe in the grains is very low (L. Nittler 2022, private communication). Therefore, we do not consider this as a strong constraint.

4.2. The ^{26}Al Signature in Presolar C-rich and O-rich Grains

In Figure 6 we show the $^{26}\text{Al}/^{27}\text{Al}$ ratio as predicted in the CCSN models. The dashed line indicates the highest values of the inferred initial $^{26}\text{Al}/^{27}\text{Al}$ ratios, inferred from the Mg isotope composition of presolar SiC type-X (SiC-X) and graphite grains with CCSN origin (Zinner 2014; Groopman et al. 2015). The dotted line represents the estimated initial $^{26}\text{Al}/^{27}\text{Al}$ ratio of the Group 4 oxides that may also originate from CCSNe (Nittler et al. 2008).

None of the models of LAW in Figure 6 reach the maximum ratio measured in Groopman et al. (2015), and only the Ne ashes (see Figure 5 for identification of the ashes) of the SIE model with 25 M_{\odot} initial mass reach an $^{26}\text{Al}/^{27}\text{Al}$ ratio higher than the maximum measured in the stardust grains. Higher ratios are also reached even deeper in the ejecta of the 15 M_{\odot} and 20 M_{\odot} SIE models. However, these regions of the ejecta are not C-rich and have a very low absolute Al abundance. Therefore, including these layers in any realistic mixing of stellar material coming from different regions of the CCSN ejecta would not affect the final Al ratio in the resulting mixture. The RIT models reach the maximum measured ratio in the H-burning ashes that are mildly C-rich. Typical abundance signatures in C-rich grains from CCSNe, e.g., the enrichment in ^{15}N and ^{28}Si , and the ^{44}Ca excess due to the radiogenic contribution by ^{44}Ti (see, e.g., Amari et al. 1992, 1995; Besmehn & Hoppe 2003), require some degree of mixing with other CCSN layers, where the ^{26}Al enrichment is lower. It is still a matter of debate which components of the ejecta shape the mixtures observed in C-rich presolar grains. They could either undergo extensive mixing with deeper Si-rich regions (e.g., from the so-called Si/S zone; Travaglio et al. 1999; Liu et al. 2018a), or more localized mixing between C-rich layers (e.g., Pignatari et al. 2013, 2015; Xu et al. 2015). Some degree of contamination or mixing with isotopically normal material without ^{26}Al has to be expected. More generally, the isotopic abundances from the RIT models would need to be compared directly with single presolar grains, to check if the ^{26}Al

enrichment can be reproduced along with other measured isotopic ratios (e.g., Liu et al. 2016; Hoppe et al. 2018).

Pignatari et al. (2015) showed that the ingestion of H in the He shell of the massive-star progenitor shortly before the onset of the CCSN explosion could potentially provide enough ^{26}Al to reproduce the most ^{26}Al -rich grains. None of the models considered in this work have developed late-H-ingestion events, and therefore we cannot fully explore the impact of these events in our study. While H ingestion in CCSN models has been identified in stellar simulations for a long time (e.g., Woosley & Weaver 1995), the quantitative impact of these events on nucleosynthetic production is still poorly explored and there remain large uncertainties. This is also due to the intrinsic difficulty of 1D models to provide robust predictions for these events (see, e.g., the discussion in Pignatari et al. 2015; Hoppe et al. 2019). We thus confirm that reproducing the high $^{26}\text{Al}/^{27}\text{Al}$ ratios in C-rich grains is still a major challenge for modern nuclear astrophysics.

Nevertheless, based on previous works, we can qualitatively expect that if H ingestion and a following explosive H-burning phase take place, the neutron burst in the He-shell material will be mitigated compared to models without H ingestion (e.g., Pignatari et al. 2015; Liu et al. 2018b). Therefore, the isotopes that are created in this region via the neutron captures relevant for this work, which include $^{25,26}\text{Mg}$ and $^{53,54}\text{Cr}$ (see Table 3) as well as $^{48,50}\text{Ti}$, may be produced with smaller efficiency. In this case, the resulting nucleosynthesis might affect our overlap regions in Table 3. We can speculate that the reduced $^{53}\text{Cr}/^{52}\text{Cr}$ and $^{54}\text{Cr}/^{52}\text{Cr}$ ratios could potentially affect the possibility for an overlap region to exist in the He shell, depending on the exact remaining abundance of these isotopes. This aspect will need to be studied in the future, possibly using a new generation of massive-star models informed by multidimensional hydrodynamics simulations of H ingestion (e.g., Clarkson & Herwig 2021).

Nittler et al. (2008) concluded that four of their 96 analyzed presolar oxide grains originated from CCSNe. The dotted line in Figure 6 is the maximum of the $^{26}\text{Al}/^{27}\text{Al}$ ratio of those four grains. All nine CCSN models shown in Figure 6 reach this maximum value in an O-rich region. In the LAW models the dotted line is reached for the 15 M_{\odot} in the C ashes. The 20 M_{\odot} and 25 M_{\odot} models reach the dotted line in the He ashes. The regions of the SIE models that reach the dotted line are, for the 15 M_{\odot} , the He ashes and the H ashes; for the 20 M_{\odot} model, the inner C ashes; and for the 25 M_{\odot} , the Ne ashes. In the RIT models, the 15 M_{\odot} model reaches the limit of Nittler et al. (2008) in the H ashes, the 20 M_{\odot} model in the C ashes, and the 25 M_{\odot} in the outer He ashes.

Therefore, in the case of these four presolar oxide grains that are assumed to have originated in CCSNe, there are extended O-rich regions consistent with the measured ^{26}Al enrichment. Thus, local or more extended mixing of different stellar layers may potentially match the observed $^{26}\text{Al}/^{27}\text{Al}$ ratio. The O isotopic ratios reported in Nittler et al. (2008) of these grains, however, are only reached in the envelope. Further analysis of all isotopic ratios obtained from these four grains is needed to conclude their region of origin.

We note that while so far only the Group 4 oxides have been suggested to originate from CCSNe, recently Hoppe et al. (2021) showed that some silicates from Group 1 and Group 2 could also be compatible with a CCSN origin, based on a comparison of their high $^{25}\text{Mg}/^{24}\text{Mg}$ ratios to CCSN models

Table 4Factors Used to Multiply the Indicated Reaction Rates from their Standard Values in the $20 M_{\odot}$ Models Considered in this Section

	$^{53}\text{Cr}(n,\gamma)^{54}\text{Cr}$	$^{54}\text{Cr}(n,\gamma)^{55}\text{Cr}$
Model 1 ^a	1	1
Model 2	1.5	1
Model 3	2	1
Model 4	1	0.5
Model 5	2	0.5
	$^{48}\text{Ti}(n,\gamma)^{49}\text{Ti}$	$^{50}\text{Ti}(n,\gamma)^{51}\text{Ti}$
Model 6	2	1
Model 7	1	0.5
Model 8	2	0.5

Note.

^a Using the values of the KaDoNiS database (Dillmann et al. 2006), which produces results very similar to those by LAW and SIE.

affected by H ingestion. More investigations are needed to define the full range of ^{26}Al enrichment and ^{26}Mg abundance signatures in all oxides and silicate grains with a possible CCSN origin.

5. Discussion

5.1. Effects of Uncertainties in Neutron-capture Reaction Rates on the Cr and Ti Ratios

By considering three different data sets of stellar models, we have derived a qualitative estimate of the effect of stellar physics uncertainties and different computational approaches. This, however, does not provide us with a systematic way to check the effect of nuclear uncertainties. We have considered these separately and we present them here.

As discussed in Section 3.1, the main channel of production of ^{53}Cr and ^{54}Cr in regions from whence the chromite grains potentially originated are neutron captures on other Cr isotopes. The final abundances of ^{53}Cr , ^{54}Cr , ^{48}Ti , and ^{50}Ti after a given neutron-flux episode are controlled mostly by their neutron-capture rates. To test how variations in these rates affect the Cr and Ti isotopic ratios, we performed several dedicated tests using the MESA stellar-evolution code, version 10398 (Paxton et al. 2011, 2013, 2015, 2018). We used the settings for a massive star as described in Brinkman et al. (2021) and considered models with an initial mass of $20 M_{\odot}$ with $Z=0.014$ evolved up to the core collapse. We chose this progenitor model for our tests because the explosion has no significant impact on the abundances in the regions relevant for our analysis. The SN explosion was not included in these tests, which is justified by the fact that the Cr isotopes in the C and He ashes are more significantly affected by the progenitor evolution than by the explosion, as shown in the Appendix.

We multiplied the neutron-capture reaction rates of interest by different constants, as indicated in Table 4. We chose variations in the direction that would help the models provide a better match to the most anomalous grain and we varied the rates by up to a factor of 2. This is larger than the up to 50% uncertainty at 2σ reported for the recommended values in the KaDoNiS database¹⁶ version 0.2 (Dillmann et al. 2006, and therefore in the JINA reaclib database, which uses KaDoNiS).

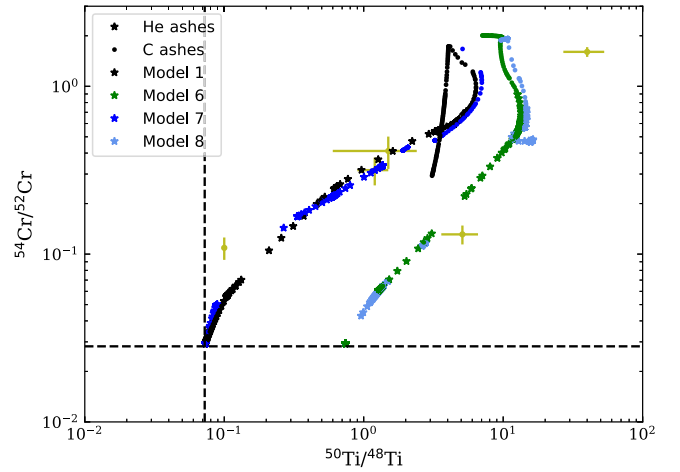


Figure 8. Same as Figure 7 but for the $^{50}\text{Ti}/^{48}\text{Ti}$ ratio resulting from the four $20 M_{\odot}$ models calculated using different Ti neutron-capture rates, and reference model Model 1. The rates used in these tests are listed in the bottom half of Table 4.

However, these reactions were measured several decades ago: these current recommended values are from Kenny et al. (1977) for the Cr isotopes, from Allen et al. (1977) for ^{48}Ti , and from Sedyshev et al. (1999) for ^{50}Ti . Therefore, it is possible that systematic uncertainties are much higher than the reported uncertainty.

Figures 7 and 8 show the results for the Cr and Ti isotopic ratios, respectively, in the C ashes and He ashes, which are the two possible sites of origin for the grains as described in Section 4. In the case of the Cr isotopic ratios, two expected main trends are visible: (i) in the models with an enhanced $^{53}\text{Cr}(n,\gamma)^{54}\text{Cr}$ rate only (Models 2 and 3), the $^{53}\text{Cr}/^{52}\text{Cr}$ ratio decreases relative to the standard Model 1, for example from a maximum in the He ashes around 0.16 to a minimum of 0.07, i.e., roughly a factor of 2; (ii) in Model 4, with the reduced $^{54}\text{Cr}(n,\gamma)^{55}\text{Cr}$ rate, the $^{54}\text{Cr}/^{52}\text{Cr}$ ratio increases relative to Model 1, for example in the C ashes from ~ 1 to ~ 2 . In the combined test (Model 5), the $^{54}\text{Cr}/^{52}\text{Cr}$ ratio increases further to ~ 3 in the C ashes compared to Model 1. Although these tests are only meant to provide a basic estimation of the impact of nuclear uncertainties, we can already derive that the uncertainties of the neutron-capture rates of Cr isotopes have a significant impact on stellar calculations. Therefore, new measurements of these neutron-capture rates are needed to reduce the uncertainty of the model predictions.

When considering the results of the Ti tests, we find that increasing the $^{48}\text{Ti}(n,\gamma)^{49}\text{Ti}$ reaction rate only (Model 6) leads to an increase of the $^{50}\text{Ti}/^{48}\text{Ti}$ ratio. Decreasing the $^{50}\text{Ti}(n,\gamma)^{51}\text{Ti}$ reaction rate only (Model 7) does not have a significant effect, because ^{50}Ti is a magic nucleus and therefore has a very low neutron-capture cross-section in both nuclear-reaction setups. As a consequence, when both rates are changed in Model 8, the result is very similar to Model 6. We also tested the case for Ti with the rates multiplied and divided by 1.5 instead of 2; the results are very similar to those obtained by using the factor of 2. The result of these reaction-rate tests concerning the Cr and Ti isotopes are used to define the boxes in Figures 3 and 4 as described in Section 4.1.

We did not test the impact of the nuclear uncertainties affecting the production of neutrons. In both the He ashes and the C ashes the $^{22}\text{Ne}(\alpha,n)^{25}\text{Mg}$ reaction is the main neutron

¹⁶ See <https://kadonis.org/>.

source. The impact of its present uncertainty on He-burning and C-burning nucleosynthesis is well studied (e.g., Kaeppeler et al. 1994; Heger et al. 2002; Pignatari et al. 2010). A more precise definition of the competing α -capture rates $^{22}\text{Ne}(\alpha, n)^{25}\text{Mg}$ and $^{22}\text{Ne}(\alpha, \gamma)^{26}\text{Mg}$ at relevant stellar temperatures is an open problem of nuclear astrophysics and has been an active line of research for many years (e.g., Longland et al. 2012; Talwar et al. 2016; Adsley et al. 2021).

5.2. Al and Mg Composition of the Core-collapse Supernova Regions as Candidate Sites of Origin of the Chromite Grains

Here we investigate the link between the Al and Mg isotopic ratios and the ^{54}Cr enrichment in the chromite grains, because of the significance of the apparent correlation between ^{54}Cr and ^{26}Mg among planetary objects. As mentioned in the Introduction (Section 1), our method in this and in the following subsection is valid only under the assumption that Al and Mg abundances are carried in the chromite grains and/or similar carriers enriched in Al and produced in the same region of the chromite grains. While the volatility of Cr and Mg in an O- and Cr-rich CCSN environment is poorly constrained, at least under early solar system conditions they might be comparable: both elements start condensation in the spinel phase and their major host phases, although different, have similar 50% condensation temperatures (Lodders 2003).

In Figure 9 we show the $^{26}\text{Al}/^{27}\text{Al}$, $^{25}\text{Mg}/^{24}\text{Mg}$, and $^{26}\text{Mg}/^{24}\text{Mg}$ ratios as a function of the mass coordinate of the three CCSN data sets. We also highlight the overlap regions listed in Table 3 as red dots, which represent the stellar zones where the Cr composition of the chromite grains is matched. The Al and Mg isotopic ratios at the locations of the red dots in Figure 9 are therefore expected to reflect the nucleosynthetic signature of these two elements in the chromite grains. This nucleosynthetic signature may also allow us to determine if the excess at atomic mass 26, observed in the solar system material to accompany the ^{54}Cr excess (Larsen et al. 2011), is due to a ^{26}Al and/or a ^{26}Mg excess.

As discussed in detail in Section 4.1, the two main regions of interest for the origin of the chromite grains are the C and the He ashes, which is where the red dots in Figure 9 are located. Specifically, for the LAW set, these are the He ashes and the center of the C ashes in the $15 M_{\odot}$ model, the He ashes in the $20 M_{\odot}$ model, and the inner C ashes in the $25 M_{\odot}$ model. For the SIE models, the red dots are the locations in the center of the C ashes in the $15 M_{\odot}$ model and the inner C ashes in the $25 M_{\odot}$ model. In the RIT models there are no overlap regions for the most anomalous grain. However, if we consider the second and third most anomalous grains, the region between 2 and 3 M_{\odot} for the enclosed mass in the $15 M_{\odot}$ RIT model provides a possible match. The composition of this region is similar to the C ashes of the SIE $25 M_{\odot}$ model, therefore in the following we do not discuss it separately.

We remind the reader that these CCSN mass regions appear to be relatively narrow, as we identified them in Section 4.1 by trying to match specifically the most anomalous observed presolar Cr-oxide grain without mixing with material of a different composition. While there is observational evidence that the composition of the ejecta can be asymmetric (e.g., Höflich 2004), mixing within the SN remnants is still poorly understood. Studies of high-density graphite grains and SiC-X grains have suggested that small-scale mixing between different inner and outer regions of a SN must occur to explain

the nucleosynthetic signatures typical of the inner layer (such as the initial presence of radioactive ^{44}Ti and excess in ^{28}Si), together with signatures from the outer layers such as the He shell (Travaglio et al. 1999; Yoshida 2007). However, Pignatari et al. (2013) matched the grains without invoking this mixing with a composition that is produced by the effect of increasing the energy of the explosion on the He shell. In addition, Schulte et al. (2021) argue that the CCSN ejecta (especially the material coming from the innermost regions of the massive star) is too energetic to condense prior to mixing with the cold interstellar medium. At the location of the red dots in the He ashes in Figure 9, the Mg isotopic ratios are roughly a couple of orders of magnitude higher than their solar values, because ^{25}Mg and ^{26}Mg are produced by the operation of the $^{22}\text{Ne}+\alpha$ reactions. This means that even if some ^{26}Al is present here, it will not influence the total sum of ^{26}Mg and ^{26}Al . Furthermore, ^{26}Al is mainly destroyed in the He ashes by the neutron-capture reactions $^{26}\text{Al}(n, p)^{26}\text{Mg}$ and $^{26}\text{Al}(n, \alpha)^{23}\text{Na}$. In the C ashes, the Mg isotopic ratios are typically below their solar values in the inner part and above solar in the outer part, with the switch being model dependent. In the SIE $15 M_{\odot}$ model, they are below their solar values in the whole C ashes. This is due to the fact that ^{24}Mg is one of the primary products of C burning, therefore the Mg isotopic ratios $^{25}\text{Mg}/^{24}\text{Mg}$ and $^{26}\text{Mg}/^{24}\text{Mg}$ decrease toward their solar values. Subsequently, in the inner part of the C ashes during the explosion not only is ^{24}Mg strongly produced, but also $^{25,26}\text{Mg}$ are destroyed via proton captures, leading to the production of ^{26}Al . Most of the red dots in the C ashes are located in the region of the C ashes where the Mg isotopic ratios are below their solar values. The exception is the $25 M_{\odot}$ model of SIE where the red dots are located at mass coordinate 4.8–5.2 M_{\odot} , which corresponds to Mg isotopic ratios a factor of a few higher than their solar values. We note that these red dots are the only ones in the C ashes that match the $^{50}\text{Ti}/^{48}\text{Ti}$ ratio.

In summary, the CCSN models predict ^{54}Cr enrichment (as signalled by the presence of the red dots) together with stable ^{25}Mg and ^{26}Mg excesses in the He ashes, while in the C ashes both $^{25}\text{Mg}/^{24}\text{Mg}$ and $^{26}\text{Mg}/^{24}\text{Mg}$ can be either higher or lower than their solar values. In the next section we compare these findings to planetary materials. We also take into consideration the possible radiogenic contribution of ^{26}Al to ^{26}Mg .

5.3. Expected Isotopic Variations in Planetary Materials

Here we compare the expected Cr and Mg isotopic compositions of the CCSN regions whose abundance compositions match that of the chromite grains, as identified in Section 4.1, to the Cr and Mg anomalies identified in planetary materials. We start by converting the predicted CCSN ejecta into commonly used variables in cosmochemistry. Then, we present mixing trajectories calculated with the CCSN ejecta and the solar composition, and compare these to the meteoritic data.

5.3.1. Converting Core-collapse Supernova Model Data to Normalized Isotope Ratios

In the following we express the ratio of the abundance N of isotope i to isotope j (N^i/N^j) from models or measurements as part per mil (δ) or per million (μ) deviations from the terrestrial

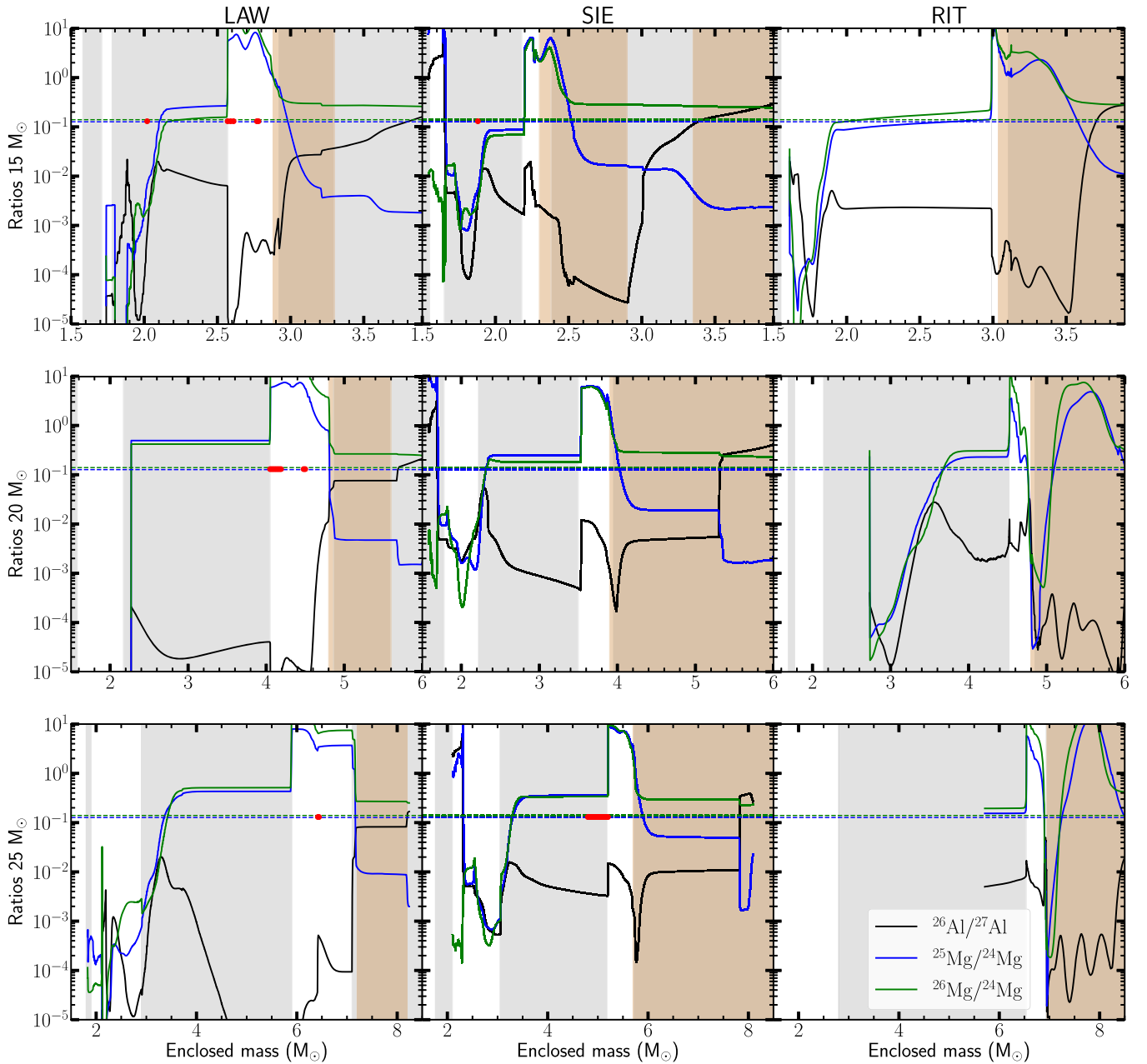


Figure 9. Ratios of $^{26}\text{Al}/^{27}\text{Al}$, $^{25}\text{Mg}/^{24}\text{Mg}$, and $^{26}\text{Mg}/^{24}\text{Mg}$ (all decayed except for ^{26}Al) for our three CCSN data sets after the explosion as a function of the mass coordinate. The 15, 20, and 25 M_{\odot} models are plotted in the top, middle, and bottom panels, respectively. The white, gray, and red bands represent the same regions as in Figure 5. The blue and green dashed lines represent the solar values for the $^{25}\text{Mg}/^{24}\text{Mg}$ and $^{26}\text{Mg}/^{24}\text{Mg}$ ratios, respectively (with values from Bizzarro et al. 2011). The red circles, plotted on the dashed lines for sake of visibility, correspond to the mass coordinates where the Cr and/or Ti isotopic ratios of the chromite grains by Nittler et al. (2018) match the ratios predicted by the models, as listed in the “Overlap” column in Table 3.

standard (TS):

$$\delta(\mu)^i N = \left(\frac{(^iN/^jN)_{\text{sample/model}}}{(^iN/^jN)_{\text{TS}}} - 1 \right) \times 10^3 (\times 10^6). \quad (1)$$

Mg isotopic ratios of planetary materials are routinely measured with precise correction for instrumental mass-dependent fractionation (IMF) using the standard “bracketing method” (Galy et al. 2001). These IMF-corrected values can be interpreted as the true values of the studied samples. They should reflect both the original nucleosynthetic mass-independent (which we indicate as $\delta^{26}\text{Mg}^*$) make-up of the analyzed materials and all the physical processes that led to natural (as

opposed to instrumental) mass-dependent isotope fractionation of the sample during its chemical history.

Unfortunately, the extent of the natural mass-dependent isotope fractionation, which we need to remove in order to obtain the original nucleosynthetic signature $\delta^{26}\text{Mg}^*$, is not precisely known (see, e.g., Wasserburg et al. 1977). For meteorites and planetary samples, it is generally assumed that all the $^{25}\text{Mg}/^{24}\text{Mg}$ deviation from the solar values as shown by the IMF-corrected values is caused by natural mass-dependent fractionation. We note that the deviations from the solar $^{25}\text{Mg}/^{24}\text{Mg}$ value are small (on % level). The normalization accounts for the maximum possible natural mass fractionation allowed by the data. The $^{26}\text{Mg}/^{24}\text{Mg}$ ratio is therefore

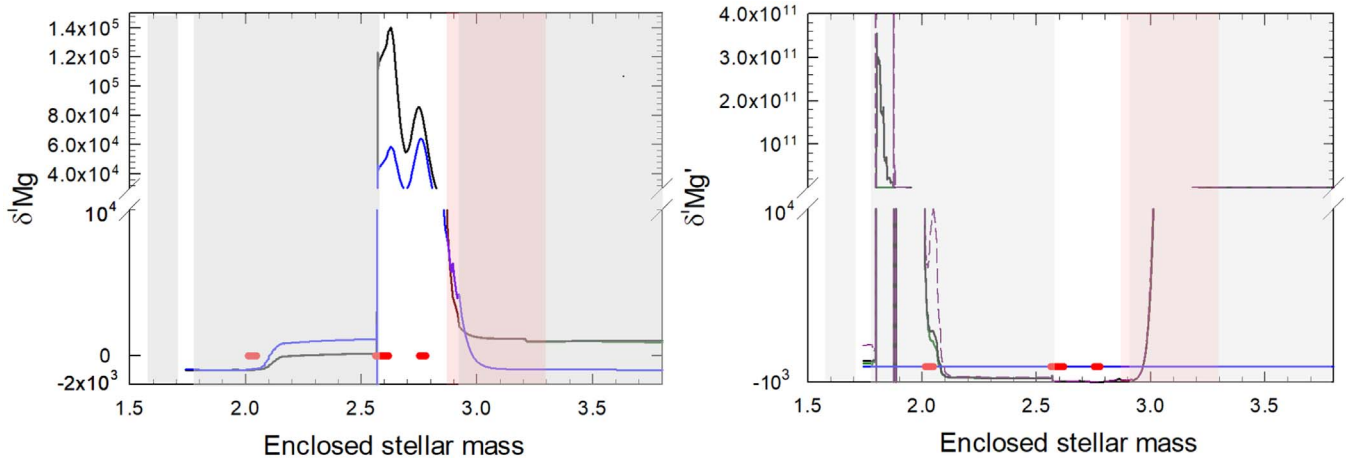


Figure 10. For the LAW 15 M_{\odot} model. Left panel: the $\delta^{25}\text{Mg}$ (blue), $\delta^{26}\text{Mg}$ (black), and $\delta^{26}\text{Mg}^*$ (green) values (where $^{26}\text{Mg}^* = ^{26}\text{Mg} + ^{26}\text{Al}$) assuming no mass fractionation of the CCSN ejecta. We show also the composition of an ejecta enriched in Al, $\delta^{26}\text{Mg}^*_{\text{E}}$ (purple dashed lines), where the Al/Mg ratio is set to 2, comparable to the abundances measured in colloidal presolar chromite grains (Dauphas et al. 2010). The ratios are expressed as δ values, corresponding to their deviation to the terrestrial ratio in part per mil (see text). Right panel: $\delta^{26}\text{Mg}'$ and $\delta^{26}\text{Mg}^{*'}_{\text{E}}$, which are the internally normalized values by assuming maximum mass-dependent fractionation of the CCSN ejecta, i.e., the $^{25}\text{Mg}/^{24}\text{Mg}$ ratio is set to the terrestrial value making $\delta^{25}\text{Mg}'$ equal to 0. This natural mass-dependent fractionation is corrected for by the exponential mass-fractionation law (see, e.g., Bizzarro et al. 2011).

corrected for natural mass-dependent fractionation by using the exponential fractionation law (Galy et al. 2001) and setting the $^{25}\text{Mg}/^{24}\text{Mg}$ ratio to the terrestrial value. This is referred to as internal normalization, which results in a $\delta^{26}\text{Mg}^*$, identified as the remaining nucleosynthetic mass-independent anomaly. This is calculated as $\delta^{26}\text{Mg}^{*'} = \delta^{26}\text{Mg} - \delta^{25}\text{Mg}/\beta$, where β is the exponent of mass fractionation (see, e.g., Bizzarro et al. 2011). Finally, we note that the original mass-independent $\delta^{26}\text{Mg}^*$ (and $\delta^{26}\text{Mg}^{*'}_{\text{E}}$) should reflect both the contribution from the nucleosynthetic ^{26}Mg and the production of radiogenic ^{26}Mg by now-extinct ^{26}Al , which is also produced by nuclear reactions in the star.

We note that in case of Cr, meteoritic and planetary data is obtained via thermal-ionization mass spectrometry using internal normalization, where instrumental and natural mass fractionation are corrected together and therefore cannot be distinguished.

A problem arises when we wish to compare model predictions to meteoritic data and convert the CCSN yields to internally normalized δ values. The issue is that the stellar $^{25}\text{Mg}/^{24}\text{Mg}$ or $^{50}\text{Cr}/^{52}\text{Cr}$ ratios are almost never equal to the terrestrial values (see Figure 9), and that in some of the nucleosynthetic sites that can produce the chromite grains, the $^{25}\text{Mg}/^{24}\text{Mg}$ ratios differ from their solar value by up to three orders of magnitude. Therefore, if we apply internal normalization using the terrestrial $^{25}\text{Mg}/^{24}\text{Mg}$ value to obtain the $\delta^{26}\text{Mg}^{*'}_{\text{E}}$ of the ejecta, we automatically imply that any deviation from the terrestrial value is due to mass fractionation, which is clearly not the case. There are two options to consider: (i) we apply internal normalization in order to treat the data the same way as in the case of laboratory measurements (see Dauphas et al. 2004); or (ii) we take the model results as the true values of the ejecta and assume no natural mass fractionation, i.e., the isotope ratio used for normalization is not taken as the terrestrial value.

In Figure 10 we show the δ -value representation of the Al and Mg isotopic ratios of the LAW 15 M_{\odot} model (see Figure 9, top-left panel) as an example. We show both $\delta^{26}\text{Mg}$ (calculated only considering the contribution of ^{26}Mg at atomic mass 26) and $\delta^{26}\text{Mg}^*$ (calculated considering the contributions of both

^{26}Mg and ^{26}Al at atomic mass 26), to highlight the impact of the abundance of ^{26}Al on the total mass budget at atomic mass 26. We show the two options above to convert the CCSN ejecta: the δ values are calculated (i) in the right panel, assuming maximum mass fractionation by setting the $^{25}\text{Mg}/^{24}\text{Mg}$ ratio to its terrestrial standard value (DSM3 standard; see Bizzarro et al. 2011), and (ii) in the left panel, assuming no mass fractionation of the ejecta.

This figure illustrates how the amplitude of isotope variations changes when using δ values instead of simple isotope ratios, as in Figure 9. Two main effects are visible: (i) when the $^{25}\text{Mg}/^{24}\text{Mg}$ ratio is lower than the terrestrial value, the ratio in Equation (1) becomes negligible and the δ value approaches -10^3 (the δ scale is not linear; see Equation (1)), e.g., as in the mass range below 2.1 M_{\odot} in the left panel; and (ii) the internally normalized $\delta^{26}\text{Mg}'$ values (i.e., when setting $^{25}\text{Mg}/^{24}\text{Mg}$ to the terrestrial value) magnify anomalies with respect to the ^{25}Mg abundance (right panel), as this is again a nonlinear transformation of data because of the exponential fractionation law. Overall, the impact of ^{26}Al at atomic mass 26 is not significant at the location of the nucleosynthetic sites of our interest (at the red dots, where the black and green lines overlap).

For the 15 M_{\odot} LAW model, the only location in the star where there is a difference between $\delta^{26}\text{Mg}'$ and $\delta^{26}\text{Mg}^{*'}_{\text{E}}$ is the inner C ashes, where the strong depletion of ^{26}Mg accompanied by the enhancement of ^{26}Al generates a separation between the δ values calculated using ^{26}Mg only (green line) or using $^{26}\text{Mg} + ^{26}\text{Al}$ (black line). However, no red dots are present in these regions of the 15 M_{\odot} LAW model, therefore, the ^{54}Cr -rich grains are not matched here. A similarly strong contribution of the ^{26}Al abundance relative to the ^{26}Mg abundance at atomic mass 26 in the calculation of the δ values shown in Figure 10 only develops in the Ne ashes, at a mass coordinate of about 1.8 M_{\odot} . We also checked the behavior of the other models and found that the contribution of ^{26}Al to atomic mass 26 also becomes relevant in the Ne ashes for the 25 M_{\odot} LAW model and all SIE models, as well as in the shell-merger region of the 15 M_{\odot} RIT model, i.e., in regions that did not produce the composition of the chromite grains. We found

one candidate site in a more central region of the C ashes in the 25 M_{\odot} SIE model, which shows $^{25,26}\text{Mg}/^{24}\text{Mg}$ ratios higher than the solar value, and while the ^{26}Al production is ongoing, its abundance relative to ^{26}Mg remains insignificant.

In addition, we show an example of a more likely scenario, where we calculate an Al-enriched $\delta^{26}\text{Mg}^*_{\text{E}}$ (purple dashed lines in Figure 10) using an Al/Mg = 2 ratio, similar to the value reported by Dauphas et al. (2010). This calculation better represents an ejecta rich in refractory oxide phases. We find that this enrichment does not play a significant role, except in the case of the C ashes when the data is internally normalized (right panel of Figure 10, where the purple dashed line peaks at around 2.05 M_{\odot}). In the regions of interest here (the red dots), instead, the maximum contribution of ^{26}Al to the total mass at atomic mass 26 even in this enriched case corresponds to an increase of at most 50%.

5.3.2. Mixing Trajectories

In Figure 11 we show the predicted trajectories of two-component mixing between the particular sites of CCSNe identified in Section 4.1 (i.e., the red dots, which denote the ejecta whose abundance composition matched the Cr isotopic signature of the presolar chromite grains) and the solar material with solar Cr and Mg abundances and terrestrial isotopic composition. For comparison, we also show the small, correlated mass-independent Mg and Cr anomalies reported in several meteorites as internally normalized $\mu^{26}\text{Mg}^*$ versus $\mu^{54}\text{Cr}'$ values from Larsen et al. (2011). Note that the data sets on Cr chondrules and CAIs are omitted because these materials are more heterogeneous, showing up to 100 ppm variation in the stable Mg isotopes and a 5% variation in the initial ^{26}Al abundance (see, e.g., Luu et al. 2019 and Larsen et al. 2020 for more details).

In general, each mixing line is a hyperbola that connects two “end-members”: the solar isotopic composition, in the origin by definition, and the isotopic composition of the specific CCSN region fitting the chromite grain composition. The curvature (K) of the line is determined by the relative abundance of the normalizing isotopes (^{52}Cr and ^{24}Mg) in the ejecta compared to the solar system value: $K = (^{52}\text{Cr}/^{24}\text{Mg})_{\text{solar}} / (^{52}\text{Cr}/^{24}\text{Mg})_{\text{CCSN}}$; see Langmuir et al. (1978) and Dauphas et al. (2004). Therefore, the line features are determined by both the isotopic composition (μ values in the plots) and the elemental composition, relative to the solar value of the CCSN ejecta. Note that the full lines are hyperbolas, but the plots are zoomed into the region of the meteoritic data, therefore they appear as linear. It is common practice to plot the mixing trajectories as symmetric lines going through the solar/terrestrial value representing not only the addition but also the subtraction or “unmixing” of a nucleosynthetic component. For clarity, here instead we only plot the mixing trajectories that result from addition of CCSN material to the solar abundances, to indicate the composition vectors toward the CCSN composition and to highlight model differences. To calculate the CCSN end-member we show results with and without mass-dependent fractionation, as outlined in the previous section. In the top panels of Figure 11 we show the trajectories derived from internal normalized model data (as in the right panel of Figure 10), and in the bottom panels of Figure 11 we show the trajectories derived from no mass fractionation in the CCSN ejecta (as in the left panel of Figure 10).

The lines in the top and bottom panels are very different from each other because in both the C ashes and He ashes the isotopic ratios that we use for internal normalization, $^{50}\text{Cr}/^{52}\text{Cr}$ and $^{25}\text{Mg}/^{24}\text{Mg}$, are very different from the solar values. For example, in the He ashes, the ^{50}Cr is completely destroyed and ^{25}Mg is produced (see the Appendix). Therefore, these normalizing isotopic ratios are at least as anomalous than the isotopic ratios we are investigating ($^{54}\text{Cr}/^{52}\text{Cr}$ and $^{26}\text{Mg}^*/^{24}\text{Mg}$). This leads to extreme transformation of the isotopic space when applying internal normalization, even resulting in a change of sign in δ and μ notation.

All the solid and dotted lines (corresponding to the C and the He ashes, respectively) are horizontal because both in the He and C ashes the abundance of Mg is much higher than the abundance of Cr, therefore the signature of the Mg isotopic composition is stronger in this representation relative to that of the Cr isotopic composition (i.e., K is between 1 and 200). We also note that the Mg isotopic signature is always dominated by the stable Mg isotopes rather than by ^{26}Al .

As mentioned in the Introduction (Section 1) and at the start of Section 5.2, there is no published study on Mg isotopes in presolar chromite grains that gives evidence that chromite grains carry anomalies in Mg isotopes. Nevertheless, Dauphas et al. (2010) reported elemental abundances in chromite grains showing variable enrichment of Al and Cr relative to Mg. Following this indication, we considered the possibility of CCSN material enriched in Al and Cr with respect to Mg, with respect to the CCSN-calculated abundances. For simplicity here we made a test using Al:Mg:Cr = 2:1:1 (dashed and dotted-dashed lines in Figure 11 for the He and C ashes, respectively), noting that this represents an enrichment for Al, because the Al/Mg ratios in the CCSN candidate site are $\simeq 0.15$, higher than the solar ratio of 0.06 but still much lower than 2, and for Cr, because the Cr/Mg ratios in the CCSN candidate sites are even lower than the solar ratio of 0.01. In these enriched cases, the K value becomes lower than 0.1 and therefore the mixing lines deviate from horizontal.

In these enriched cases for the C ashes, the mixing lines appear as almost vertical as they are dominated by the increased relative abundance of ^{52}Cr in this part of the CCSN ejecta (see the Appendix). None of them match the correlation displayed by the meteoritic data. This C-ashes material could still be in agreement with other interpretations of the measured planetary Mg isotopic data, suggesting an homogeneous protoplanetary disk for Mg isotopes on a level of a few parts per million (ppm) (e.g., Jacobsen et al. 2008; Kita et al. 2013; Luu et al. 2019).

In the case of the enriched He ashes, the $^{52}\text{Cr}/^{24}\text{Mg}$ ratio relative to the solar ratio is less extreme and the highly variable μ values from the isotopic composition dominate the mixing trajectories. In the top panels in Figure 11, where we use internal normalization, the trajectories match the meteoritic trend only with negative μ values. This solution, however, would be inconsistent with our assumption that the observed anomalies are carried by refractory CCSN grains because such grains would not be preferentially destroyed in the inner solar system, relative to less refractory ISM dust. Therefore, their presence should result in positive anomalies. In the bottom panels, instead, where we assume that the mass fractionation of the ejecta is negligible, the 15 and 20 M_{\odot} LAW models may generate the observed trend via mixing or unmixing of a positive CCSN component suggested by Larsen et al. (2011).

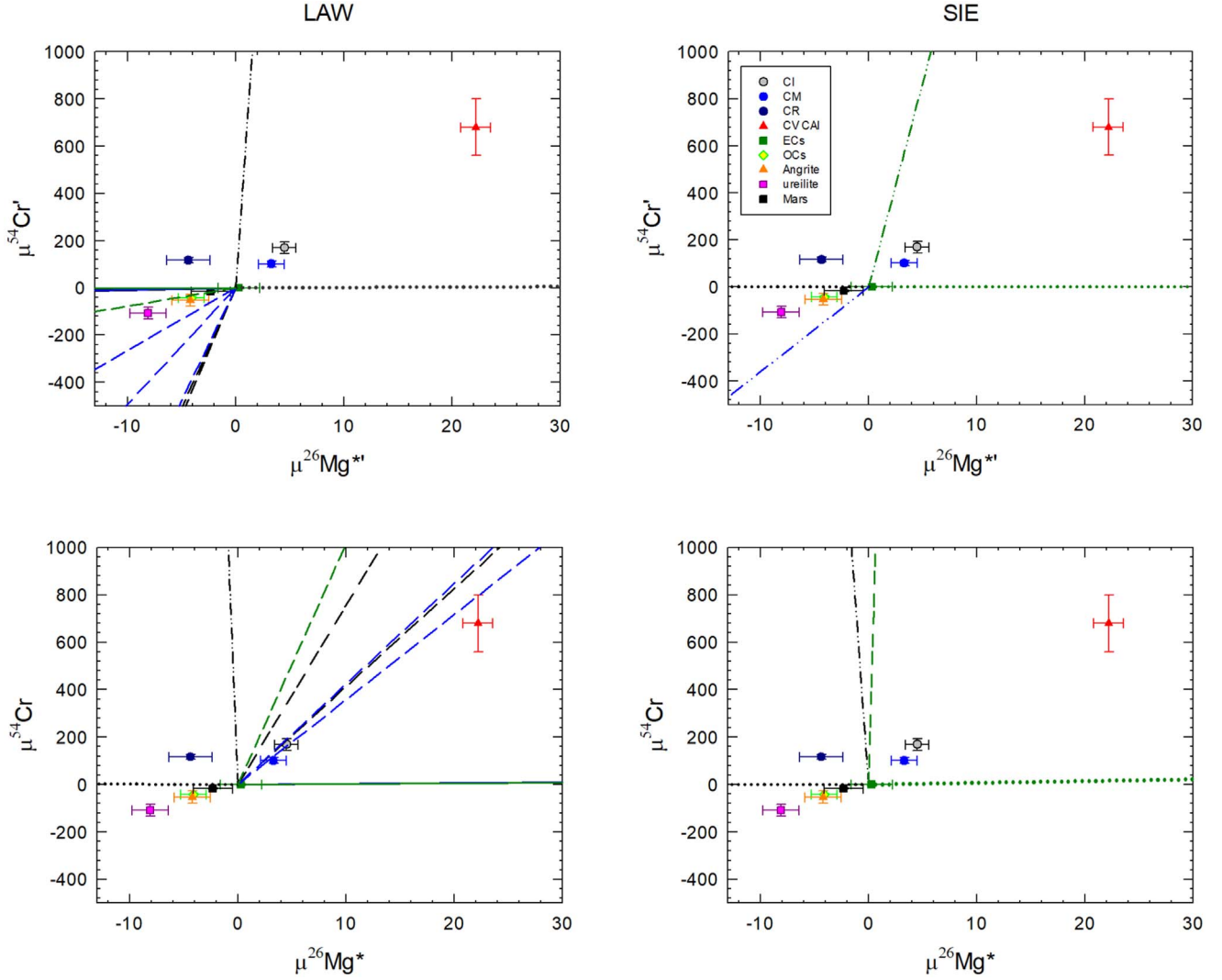


Figure 11. $\mu^{54}\text{Cr}'$ and $\mu^{26}\text{Mg}^{*+}$ values from meteoritic data (colored symbols with 2σ error bars, see legend, from Larsen et al. 2011) and predicted trajectories (lines) of $\mu^{54}\text{Cr}'$ vs. $\mu^{26}\text{Mg}^{*+}$ (top panels) and $\mu^{54}\text{Cr}$ vs. $\mu^{26}\text{Mg}^*$ (bottom panels) obtained by mixing between a solar component and the CCSN ejecta of the regions identified in Section 4.1 (i.e., the red dots) for the LAW and SIE models (left and right panels, respectively). The colors of the mixing lines represent models for different stellar masses as before, i.e., black, blue, and green are used for the 15, 20, and 25 M_{\odot} , respectively. The C ashes are indicated by the dotted lines and the He ashes by the solid lines. The dashed and dotted-dashed lines were calculated with Al- and Cr-enriched composition in the He and C ashes, respectively. Top panels: the mass-independent isotopic composition $\mu^{54}\text{Cr}'$ and $\mu^{26}\text{Mg}^{*+}$ values of the CCSN ejecta were calculated by setting the $^{52}\text{Cr}/^{50}\text{Cr}$ and $^{25}\text{Mg}/^{24}\text{Mg}$ ratios to the NIST979 and DSM3 terrestrial standard values for Cr and Mg, respectively (Qin et al. 2010; Bizzarro et al. 2011). To follow the data reduction of meteorite measurements, we applied the exponential law to correct for mass fractionation (Russell et al. 1978). Bottom panels: the CCSN ejecta are assumed to retain their isotopic composition, i.e., mass-dependent isotope fractionation is negligible. $\mu^{54}\text{Cr}$ and $\mu^{26}\text{Mg}^*$ are calculated by simple deviation of their isotopic ratio values from the terrestrial standard values in ppm units without internal normalization.

Note that the composition of the SIE He ashes is just outside the border of the box defined in Figure 4, therefore they are not included in this plot, but if they did they would behave similarly to the LAW He ashes.

6. Conclusions

We presented a detailed analysis of the production of the Al, Mg, and Cr isotopes from CCSN models with nonrotating, single-star progenitors. We compared the total isotopic yields between seven CCSN data sets and we compared the isotopic composition as a function of mass coordinate from three CCSN sets to the isotopic composition measured in meteoritic stardust grains. We found potential nucleosynthetic origin sites of the chromite grains presented in Nittler et al. (2018), and evaluated the contribution at atomic mass 26 at those potential sites.

Concerning the total CCSN yields, we found that the seven CCSN data sets are mostly comparable to each other for the nine isotopes of interest: $^{24,25,26}\text{Mg}$, $^{26,27}\text{Al}$, and $^{50,52,53,54}\text{Cr}$. The main differences are due to different mass cuts (mainly driving variations in the abundances of Cr isotopes), the occurrence of a shell merger in the 15 M_{\odot} RIT models, and structural differences in the progenitors between the LAW and SIE data sets. Based on a detailed analysis of the production sites of these isotopes in the different models, we are confident that our findings are representative of most 1D CCSN models of solar metallicity.

We compared the CCSN models to the composition of the chromite grain most anomalous in ^{54}Cr , 2_37, including an estimate of the uncertainties due to neutron-capture rates on ^{53}Cr , ^{54}Cr , ^{48}Ti , and ^{50}Ti , based on our sensitivity tests.

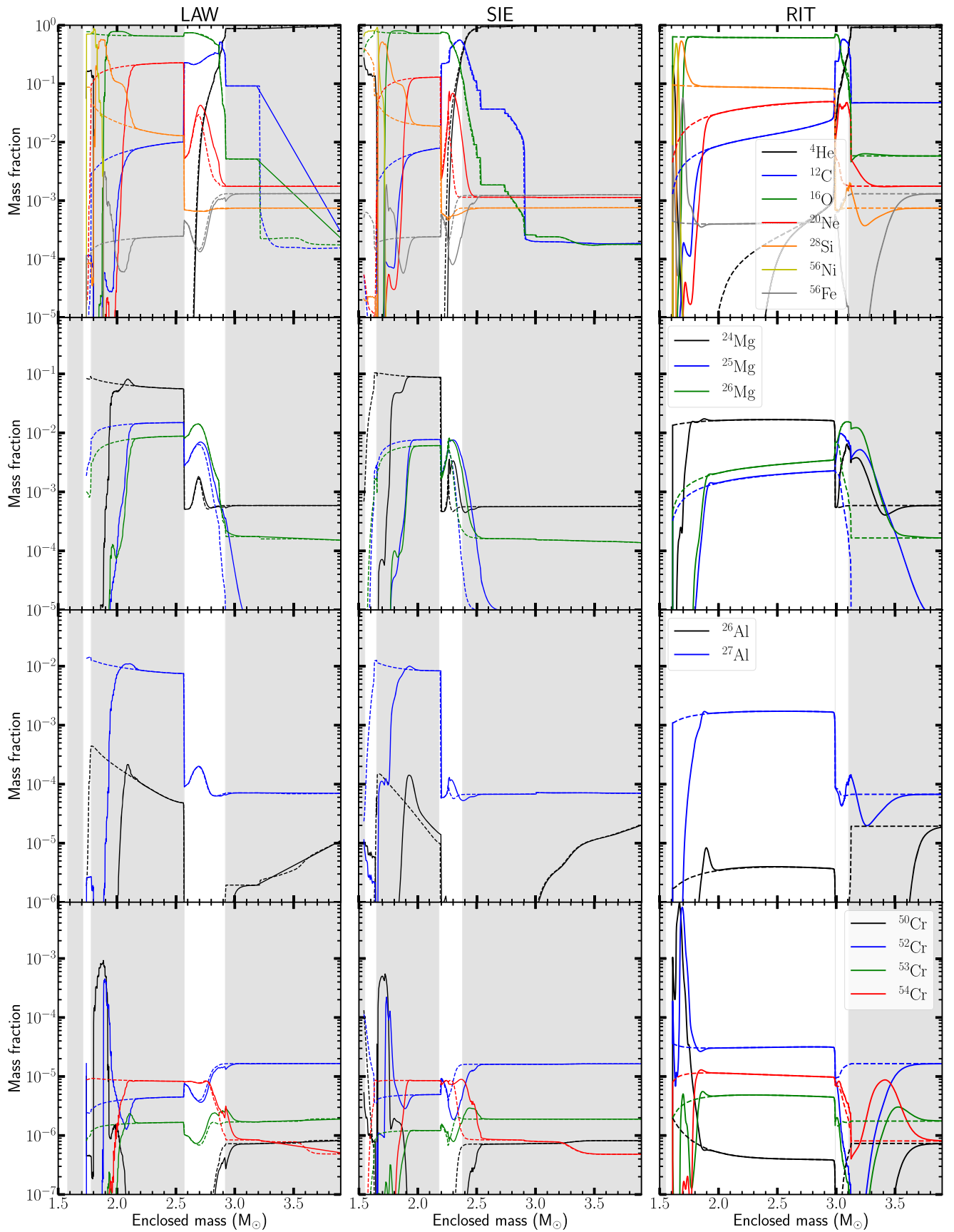


Figure A1. Nondecayed mass fraction profiles of the $15 M_{\odot}$ models of the LAW, SIE, and RIT data sets. The dashed lines are the mass fractions in the progenitor, the solid lines show the fractions after the CCSN.

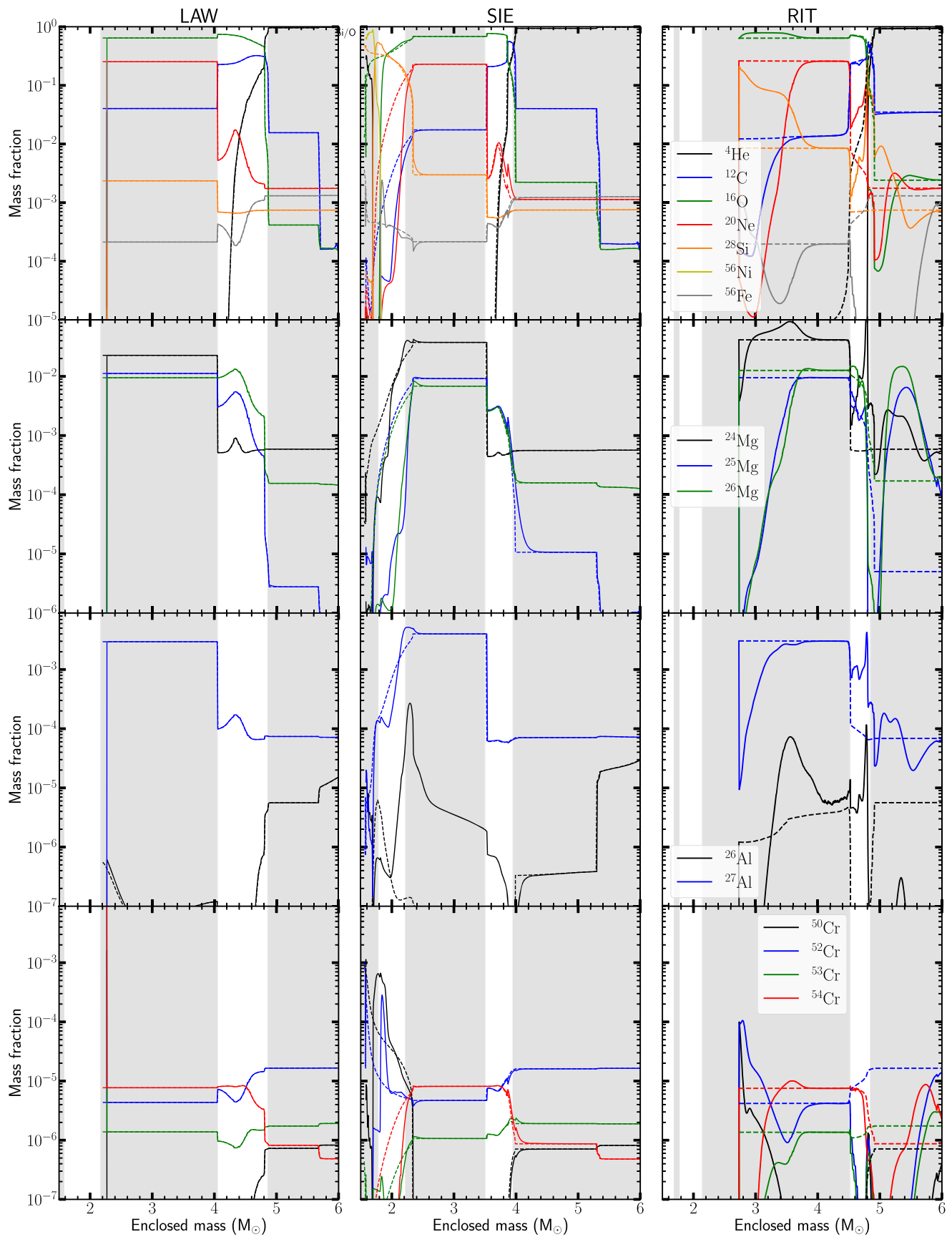


Figure A2. Nondecayed mass fraction profiles of the 20 M_{\odot} models of the LAW, SIE, and RIT data sets. The dashed lines are the mass fractions in the progenitor, the solid lines show the fractions after the CCSN.

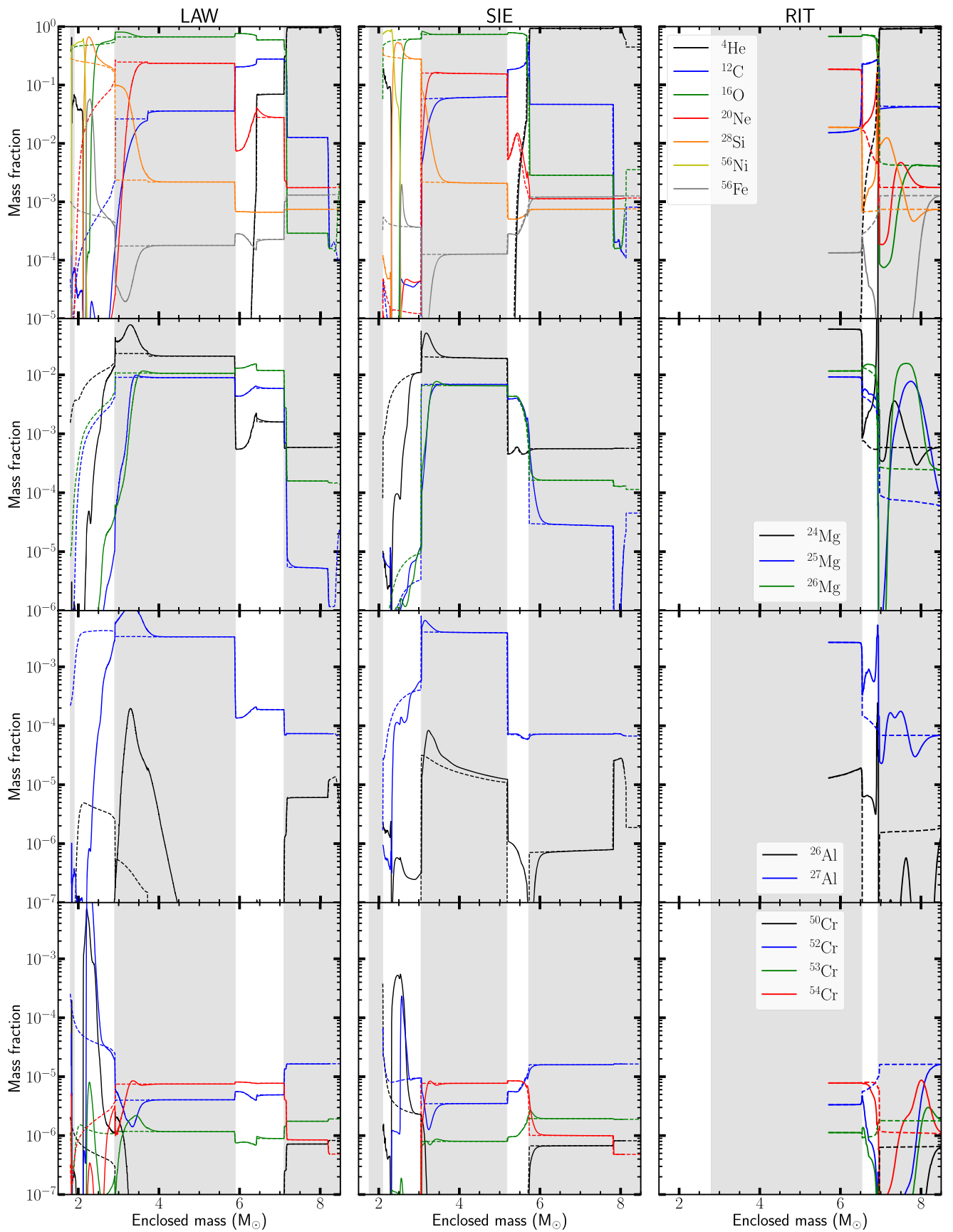


Figure A3. Nondecayed mass fraction profiles of the 25 M_{\odot} models of the LAW, SIE, and RIT data sets. The dashed lines are the mass fractions in the progenitor, the solid lines show the fractions after the CCSN.

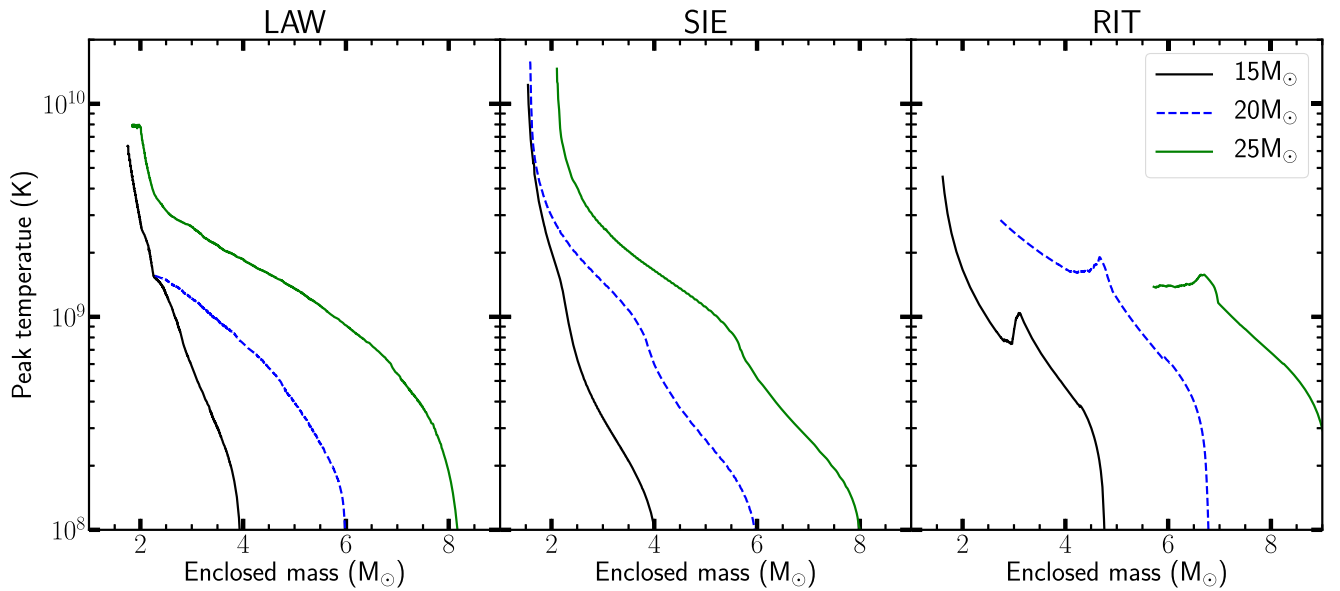


Figure A4. Temperature profiles for the explosions in all three CCSN model sets. The extra peaks in the RIT models (see, e.g., in the $15 M_{\odot}$ model at mass coordinate $3.2 M_{\odot}$) are due to the analytic explosion model, which allows the velocity and thus temperature to increase when the shock decelerates (Pignatari et al. 2016). These peaks allow for explosive He burning in the H ashes.

For all models, we were able to identify mass regions within the CCSN ejecta where the $^{54}\text{Cr}/^{52}\text{Cr}$ and $^{53}\text{Cr}/^{52}\text{Cr}$ ratios matched; however, the situation was more complicated for the ratios including the atomic mass 50 isotopes. Only in five out of nine models could we find a complete solution and only in small regions of the CCSN ejecta (see Table 3). These solutions are all located in either the C ashes or the He ashes in all the models of LAW and in the 15 and $25 M_{\odot}$ models of SIE. The three RIT models did not show any overlap regions with grain 2_37. The regions that match the $^{50}\text{Cr}/^{52}\text{Cr}$ ratio of 2_37, and overlap with the regions matching its $^{54}\text{Cr}/^{52}\text{Cr}$ and $^{53}\text{Cr}/^{52}\text{Cr}$ ratios, are located in the C ashes. In contrast, the regions that overlap with the $^{50}\text{Ti}/^{48}\text{Ti}$ ratio are located in the He ashes, with only one case in the C ashes.

When we consider the second and third most anomalous grains, we find again that both the C and He ashes from the LAW and SIE models can match these grains; however, in these cases the signal at atomic mass 50 must always come from ^{50}Ti . Furthermore, when considering these two grains we also find that the shell-merger region in the $15 M_{\odot}$ RIT model could be a match, in which case the isotope at atomic mass 50 could be either ^{50}Cr or ^{50}Ti .

We found that adding or not adding the radioactive ^{53}Mn into ^{53}Cr does not significantly affect the results. This is different from Jones et al. (2019b), who found that for electron-capture SN ejecta the partial inclusion of ^{53}Mn in ^{53}Cr is crucial to match the values of grain 2_37.

We conclude that the chromite grains analyzed by Nittler et al. (2018) could have originated from CCSNe. We emphasize that CCSNe are the most frequent stellar events among the production sites considered so far (Nittler et al. 2018; Jones et al. 2019a), thus making them likely candidates as the origin of these grains.

The Al isotopic data from SiC-X grains are believed to have originated from CCSNe (Groopman et al. 2015). We confirm, however, that standard CCSN models do not produce enough ^{26}Al in their C-rich ejecta to match these grains (see Figure 6). Therefore, mixing of layers within CCSN models and/or a

proton ingestion into the He shell (Pignatari et al. 2015) are needed to match the grain data. For the few oxide grains of Group 4 that also potentially originate from CCSNe (Nittler et al. 2008), we could match their Al isotopic ratios; however, a multielement isotope analysis is needed to evaluate the origin of those grains.

In the candidate regions within the He ashes that reproduce the Cr isotopic ratios of the presolar chromite grains, the $^i\text{Mg}/^{24}\text{Mg}$ ratios are orders of magnitude higher than the solar ratio. Here, ^{26}Al is being destroyed by neutron-capture reactions and has little effect on the total abundance at atomic mass 26. In the candidate regions within the C ashes, the $^i\text{Mg}/^{24}\text{Mg}$ ratios of the inner regions are orders of magnitude lower than the solar values, due to the production of ^{24}Mg by C burning and the partial depletion of ^{25}Mg and ^{26}Mg by neutron capture and proton capture. While the abundance of ^{26}Al is more significant at these latter sites, it never dominates the production at atomic mass 26. Since presolar chromite grains alone may drive the variation of Cr isotopes in the protoplanetary disk, we conclude that the ejecta carrying the chromite grains could have also generated nucleosynthetic ^{26}Mg isotopic variation in the disk, and such variation would be dominated by nonradiogenic, stable Mg isotopic anomalies.

We compared Cr and Mg isotopic anomalies measured in meteorites and planetary materials with our candidate sites from the CCSN models, and derived the expected mixing trajectories between the solar and the CCSN reservoirs under the simple assumption that such Al and Mg abundances are carried within the chromite grains and/or similar carriers enriched in Al. When considering CSSN refractory material enriched in Al and Cr relative to Mg, as suggested by the data of Dauphas et al. (2010), we found that the ejecta of the C ashes does not generate significant Mg isotopic variations due to the extreme ^{52}Cr abundances relative to ^{24}Mg . The ejecta of the He ashes, instead, can generate a trend similar to the apparent Cr versus Mg isotopic heterogeneity. This trend is positive, as required under our assumption of refractory carriers, only if the

CCSN material is not double normalized. The validity of such a comparison method requires further investigation.

Future measurements of chromite grains with resonant ionisation mass spectrometry (RIMS; Stephan et al. 2016) are needed to identify if the signal at atomic mass 50 is related to ^{50}Cr from the C ashes or ^{50}Ti from the He ashes, since this instrument can in principle extract isotopes of a single element and avoid isobaric interference during the analysis. Furthermore, to study the link between stardust grains and planetary objects and investigate the possible ^{26}Al heterogeneity of the protoplanetary disk, we have assumed here that Al and Mg abundances are also carried in the chromite grains and/or similar carriers enriched in Al. This assumption needs to be investigated via future Mg isotope study of the ^{54}Cr -rich chromite grains. New measurements of the neutron-capture cross-sections for the Cr and Ti isotopes are also required to improve the accuracy of CCSN predictions. Finally, SN models based on self-consistent multidimensional simulations are needed to reduce the uncertainties that result from parameterized mass cuts and explosion energies.

We thank Larry Nittler for discussion and for sharing unpublished Fe data. This research is supported by the ERC Consolidator Grant (Hungary) funding scheme (Project RADIOSTAR, G.A. n. 724560). We thank the ChETEC COST Action (CA16117), supported by the European Cooperation in Science and Technology, and the IReNA network supported by NSF AccelNet. This work was supported in part by the European Union ChETEC-INFRA (project No. 101008324). T.L. and M.P. acknowledge significant support from NuGrid from STFC (through the University of Hull's Consolidated grant ST/R000840/1) and ongoing access to viper, the University of Hull High Performance Computing Facility. A.S. acknowledges support from the U.S. Department of Energy through grant No. DE-FG02-87ER40328 (UM), Office of Science, Office of Nuclear Physics and Office of Advanced Scientific Computing Research, Scientific Discovery through Advanced Computing (SciDAC) program. Research at Oak Ridge National Laboratory is supported under contract DE-AC05-00OR22725 from the U.S. Department of Energy to UT-Battelle, LLC. M.P. thanks support from the National Science Foundation (NSF) under grant No. PHY-1430152 (JINA Center for the Evolution of the Elements), and from the "Lendulet-2014" Program of the Hungarian Academy of Sciences (Hungary).

Appendix

Figures Showing the Production and Destruction of the Mg, Al, and Cr Isotopes of Interest

In this section we show in Figures 12–14 the mass fractions of the three data sets of Lawson et al. (2022), Sieverding et al. (2018), and Ritter et al. (2018) of the progenitor and the CCSN model as a function of mass coordinate. For each data set we show four figures for the three initial masses, being 15, 20 and $25 M_{\odot}$: the top panel shows the stellar structure, and includes seven isotopes that allow us to identify the various burning phases within the progenitor and the explosion following the nomenclature as presented in Section 2.5. The second panel shows the Mg isotopes, the third panel the Al isotopes, and the fourth panel shows the Cr isotopes as a function of mass coordinate. In Figure A4 we show the temperatures in the

CCSN models, which helps with identifying the differences in the nucleosynthesis between the nine CCSN models.

ORCID iDs

Jacqueline den Hartogh  <https://orcid.org/0000-0003-1976-9947>

Maria K. Petö  <https://orcid.org/0000-0003-4831-9304>

Thomas Lawson  <https://orcid.org/0000-0002-1609-6938>

Andre Sieverding  <https://orcid.org/0000-0001-8235-5910>

Hannah Brinkman  <https://orcid.org/0000-0002-7634-2432>

Marco Pignatari  <https://orcid.org/0000-0002-9048-6010>

Maria Lugaro  <https://orcid.org/0000-0002-6972-3958>

References

- Adley, P., Battino, U., Best, A., et al. 2021, *PhRvC*, 103, 015805
- Aerts, C., Mathis, S., & Rogers, T. M. 2019, *ARA&A*, 57, 35
- Allen, B., Boldeman, J., Musgrove, A. L., & Macklin, R. 1977
- Amari, S., Hoppe, P., Zinner, E., & Lewis, R. S. 1992, *ApJL*, 394, L43
- Amari, S., Zinner, E., & Lewis, R. S. 1995, *ApJL*, 447, L147
- Anders, E., & Grevesse, N. 1989, *GeCoA*, 53, 197
- Andrews, S., Fryer, C., Even, W., Jones, S., & Pignatari, M. 2020, *ApJ*, 890, 35
- Belczynski, K., Klencki, J., Fields, C. E., et al. 2020, *A&A*, 636, A104
- Besmehn, A., & Hoppe, P. 2003, *GeCoA*, 67, 4693
- Bizzarro, M., Paton, C., Larsen, K., et al. 2011, *J. Anal. At. Spectrom.*, 26, 565
- Brasser, R., & Mojszis, S. J. 2020, *NatAs*, 4, 492
- Brinkman, H. E., den Hartogh, J. W., Doherty, C. L., Pignatari, M., & Lugaro, M. 2021, *ApJ*, 923, 47
- Budde, G., Burkhardt, C., Brennecke, G. A., et al. 2016, *E&PSL*, 454, 293
- Burkhardt, C., Dauphas, N., Hans, U., Bourdon, B., & Kleine, T. 2019, *GeCoA*, 261, 145
- Burkhardt, C., Kleine, T., Dauphas, N., & Wieler, R. 2012, *E&PSL*, 357, 298
- Burrows, A. 2013, *RvMP*, 85, 245
- Chieffi, A., Limongi, M., & Straniero, O. 1998, *ApJ*, 502, 737
- Clarkson, O., & Herwig, F. 2021, *MNRAS*, 500, 2685
- Collins, C., Müller, B., & Heger, A. 2018, *MNRAS*, 473, 1695
- Côté, B., Jones, S., Herwig, F., & Pignatari, M. 2020, *ApJ*, 892, 57
- Couch, S. M., Warren, M. L., & O'Connor, E. P. 2020, *ApJ*, 890, 127
- Curtis, S., Ebinger, K., Fröhlich, C., et al. 2018, *ApJ*, 870, 2
- Curtis, S., Ebinger, K., Fröhlich, C., et al. 2019, *ApJ*, 870, 2
- Dauphas, N., Cook, D. L., Sacarabany, A., et al. 2008, *ApJ*, 686, 560
- Dauphas, N., Davis, A. M., Marty, B., & Reisberg, L. 2004, *E&PSL*, 226, 465
- Dauphas, N., Marty, B., & Reisberg, L. 2002, *ApJ*, 565, 640
- Dauphas, N., Remusat, L., Chen, J. H., et al. 2010, *ApJ*, 720, 1577
- den Hartogh, J. W., Hirschi, R., Lugaro, M., et al. 2019, *A&A*, 629, A123
- Dillmann, I., Heil, M., Käppeler, F., et al. 2006, in *AIP Conf. Ser.* 819, Capture Gamma-Ray Spectroscopy and Related Topics, ed. A. Woehr & A. Aprahamian (New York: AIP), 123
- Fryer, C. L. 2009, *ApJ*, 699, 409
- Fryer, C. L., Andrews, S., Even, W., Heger, A., & Safi-Harb, S. 2018, *ApJ*, 856, 63
- Fryer, C. L., Belczynski, K., Wiktorowicz, G., et al. 2012, *ApJ*, 749, 91
- Fryer, C. L., Woosley, S. E., & Hartmann, D. H. 1999, *ApJ*, 526, 152
- Galy, A., Belshaw, N. S., Halicz, L., & O'Nions, R. K. 2001, *IJMSp*, 208, 89
- Grevesse, N., & Noels, A. 1993, in *Origin and Evolution of the Elements*, ed. N. Prantzos, E. Vangioni-Flam, & M. Casse (Singapore: World Scientific), 15
- Groopman, E., Zinner, E., Amari, S., et al. 2015, *ApJ*, 809, 31
- Hartmann, D., Woosley, S. E., & El Eid, M. F. 1985, *ApJ*, 297, 837
- Heger, A., Fryer, C. L., Woosley, S. E., Langer, N., & Hartmann, D. H. 2003, *ApJ*, 591, 288
- Heger, A., & Woosley, S. E. 2010, *ApJ*, 724, 341
- Heger, A., Woosley, S. E., Rauscher, T., Hoffman, R. D., & Boyes, M. M. 2002, *NewAR*, 46, 463
- Helled, R., Bodenheimer, P., Podolak, M., et al. 2014, in *Protostars and Planets VI*, ed. H. Beuther et al. (Tucson: Univ. Arizona Press), 643
- Herant, M., Benz, W., Hix, W. R., Fryer, C. L., & Colgate, S. A. 1994, *ApJ*, 435, 339
- Hibiya, Y., Iizuka, T., & Enomoto, H. 2019, in *82nd Annual Meeting of The Meteoritical Society*, 82 (New York: Wiley), 6370
- Höflich 2004, *Cosmic Explosions in Three Dimensions: Asymmetries in Supernovae and Gamma-Ray Bursts*, Cambridge Contemporary

- Astrophysics (Cambridge: Cambridge Univ. Press) doi:10.1017/CBO9780511536236
- Hoppe, P., Leitner, J., Kodolányi, J., & Vollmer, C. 2021, *ApJ*, **913**, 10
- Hoppe, P., Pignatari, M., Kodolányi, J., Gröner, E., & Amari, S. 2018, *Geochim. Cosmochim. Acta*, **221**, 182
- Hoppe, P., Stancliffe, R. J., Pignatari, M., & Amari, S. 2019, *ApJ*, **887**, 8
- Jacobsen, B., Yin, Q.-z., Moynier, F., et al. 2008, *E&PSL*, **272**, 353
- Jacquet, E., Pignatale, F. C., Chaussidon, M., & Charnoz, S. 2019, *ApJ*, **884**, 32
- Janka, H.-T., Melson, T., & Summa, A. 2016, *ARNPS*, **66**, 341
- Jones, S., Röpke, F. K., Fryer, C., et al. 2019a, *A&A*, **622**, A74
- Jones, S. W., Möller, H., Fryer, C. L., et al. 2019b, *MNRAS*, **485**, 4287
- Kaeppler, F., Wiescher, M., Giesen, U., et al. 1994, *ApJ*, **437**, 396
- Karakas, A. I., & Lugaro, M. 2016, *ApJ*, **825**, 26
- Kenny, M., Macklin, R., Halperin, J., et al. 1977
- Kita, N. T., Yin, Q.-Z., MacPherson, G. J., et al. 2013, *M&PS*, **48**, 1383
- Kleine, T., Budde, G., Burkhardt, C., et al. 2020, *SSRv*, **216**, 55
- Kruijjer, T. S., Burkhardt, C., Budde, G., & Kleine, T. 2017, *PNAS*, **114**, 6712
- Langer, N. 2012, *ARA&A*, **50**, 107
- Langmuir, C. H., Vocke, R. D., Hanson, G. N., & Hart, S. R. 1978, *E&PSL*, **37**, 380
- Larsen, K. K., Trinquier, A., Paton, C., et al. 2011, *ApJL*, **735**, L37
- Larsen, K. K., Wielandt, D., Schiller, M., Krot, A. N., & Bizzarro, M. 2020, *E&PSL*, **535**, 116088
- Limongi, M., & Chieffi, A. 2003, *ApJ*, **592**, 404
- Lawson, T. V., Pignatari, M., Stancliffe, R. J., et al. 2022, *MNRAS*, **511**, 886
- Limongi, M., & Chieffi, A. 2018, *ApJS*, **237**, 13
- Liu, N., Nittler, L. R., Alexander, C. M. O. D., & Wang, J. 2018a, *SciA*, **4**, eaao1054
- Liu, N., Nittler, L. R., O'D. Alexander, C. M., et al. 2016, *ApJ*, **820**, 140
- Liu, N., Stephan, T., Boehnke, P., et al. 2018b, *ApJ*, **855**, 144
- Lodders, K. 2003, *ApJ*, **591**, 1220
- Longland, R., Iliadis, C., & Karakas, A. I. 2012, *PhRvC*, **85**, 065809
- Luu, T.-H., Hin, R. C., Coath, C. D., & Elliott, T. 2019, *E&PSL*, **522**, 166
- Meyer, B. S., Weaver, T. A., & Woosley, S. E. 1995, *Metic*, **30**, 325
- Mishra, K. K., & Chaussidon, M. 2014, *E&PSL*, **390**, 318
- Müller, B. 2016, *PASA*, **33**, e048
- Müller, B. 2020, *LRCA*, **6**, 3
- Nanne, J. A. M., Nimmo, F., Cuzzi, J. N., & Kleine, T. 2019, *E&PSL*, **511**, 44
- Nittler, L. R., Alexander, C. M. O., Gallino, R., et al. 2008, *ApJ*, **682**, 1450
- Nittler, L. R., O'D. Alexander, C. M., Liu, N., & Wang, J. 2018, *ApJL*, **856**, L24
- Parikh, A., José, J., Seitzzahl, I. R., & Röpke, F. K. 2013, *A&A*, **557**, A3
- Paxton, B., Bildsten, L., Dotter, A., et al. 2011, *ApJS*, **192**, 3
- Paxton, B., Cantiello, M., Arras, P., et al. 2013, *ApJS*, **208**, 4
- Paxton, B., Marchant, P., Schwab, J., et al. 2015, *ApJS*, **220**, 15
- Paxton, B., Schwab, J., Bauer, E. B., et al. 2018, *ApJS*, **234**, 34
- Perego, A., Hempel, M., Fröhlich, C., et al. 2015, *ApJ*, **806**, 275
- Pignatale, F. C., Charnoz, S., Chaussidon, M., & Jacquet, E. 2018, *ApJL*, **867**, L23
- Pignatale, F. C., Jacquet, E., Chaussidon, M., & Charnoz, S. 2019, *ApJ*, **884**, 31
- Pignatari, M., Gallino, R., Heil, M., et al. 2010, *ApJ*, **710**, 1557
- Pignatari, M., Herwig, F., Hirschi, R., et al. 2016, *ApJS*, **225**, 24
- Pignatari, M., Wiescher, M., Timmes, F. X., et al. 2013, *ApJL*, **767**, L22
- Pignatari, M., Zinner, E., Hoppe, P., et al. 2015, *ApJL*, **808**, L43
- Poole, G. M., Rehkämper, M., Coles, B. J., Goldberg, T., & Smith, C. L. 2017, *E&PSL*, **473**, 215
- Qin, L., Alexander, C. M. O. D., Carlson, R. W., Horan, M. F., & Yokoyama, T. 2010, *GeCoA*, **74**, 1122
- Rauscher, T., Heger, A., Hoffman, R. D., & Woosley, S. E. 2002, *ApJ*, **576**, 323
- Regelous, M., Elliott, T., & Coath, C. D. 2008, *E&PSL*, **272**, 330
- Ritter, C., Herwig, F., Jones, S., et al. 2018, *MNRAS*, **480**, 538
- Russell, W. A., Papanastassiou, D. A., & Tombrello, T. A. 1978, *GeCoA*, **42**, 1075
- Sarangi, A., & Cherchneff, I. 2015, *A&A*, **575**, A95
- Schiller, M., Bizzarro, M., & Fernandes, V. A. 2018, *Natur*, **555**, 507
- Schulte, J., Bose, M., Young, P. A., & Vance, G. S. 2021, *ApJ*, **908**, 38
- Sedyshev, P. V., Mohr, P., Beer, H., et al. 1999, *PhRvC*, **60**, 054613
- Sieverding, A., Martínez-Pinedo, G., Huther, L., Langanke, K., & Heger, A. 2018, *ApJ*, **865**, 143
- Stephan, T., Trappitsch, R., Davis, A. M., et al. 2016, *IJMSp*, **407**, 1
- Sukhbold, T., Ertl, T., Woosley, S. E., Brown, J. M., & Janka, H. T. 2016, *ApJ*, **821**, 38
- Sukhbold, T., Woosley, S. E., & Heger, A. 2018, *ApJ*, **860**, 93
- Talwar, R., Adachi, T., Berg, G. P. A., et al. 2016, *PhRvC*, **93**, 055803
- Travaglio, C., Gallino, R., Amari, S., et al. 1999, *ApJ*, **510**, 325
- Trinquier, A., Birck, J.-L., & Allègre, C. J. 2007, *ApJ*, **655**, 1179
- Trinquier, A., Elliott, T., Ulfbeck, D., et al. 2009, *Sci*, **324**, 374
- Van Kooten, E. M. M. E., Wielandt, D., Schiller, M., et al. 2016, *PNAS*, **113**, 2011
- Wanajo, S., Janka, H.-T., & Müller, B. 2013, *ApJL*, **767**, L26
- Warren, P. H. 2011, *E&PSL*, **311**, 93
- Wasserburg, G. J., Lee, T., & Papanastassiou, D. A. 1977, *GeoRL*, **4**, 299
- Weaver, T. A., Zimmerman, G. B., & Woosley, S. E. 1978, *ApJ*, **225**, 1021
- Woosley, S. E. 1997, *ApJ*, **476**, 801
- Woosley, S. E., Arnett, W. D., & Clayton, D. D. 1973, *ApJS*, **26**, 231
- Woosley, S. E., & Heger, A. 2007, *PhR*, **442**, 269
- Woosley, S. E., Heger, A., & Weaver, T. A. 2002, *RvMP*, **74**, 1015
- Woosley, S. E., & Weaver, T. A. 1995, *ApJS*, **101**, 181
- Xu, Y., Zinner, E., Gallino, R., et al. 2015, *ApJ*, **799**, 156
- Yoshida, T. 2007, *ApJ*, **666**, 1048
- Zhang, W., Woosley, S. E., & Heger, A. 2008, *ApJ*, **679**, 639
- Zinner, E. 2014, in *Presolar Grains*, ed. A. M. Davis, Vol. 1 (Amsterdam: Elsevier), 181